The Astrophysical Journal, 979:139 (21pp), 2025 February 1 https://doi.org/10.3847/1538-4357/ad98e7

What Can DKIST/DL-NIRSP Tell Us about Quiet-Sun Magnetism?

Jiayi Liu (刘嘉奕)[1,5], Xudong Sun (孙旭东)[2], Peter W. Schuck[3], and Sarah A. Jaeggli[4]
[1] Institute for Astronomy, University of Hawai'i at Mānoa, 2680 Woodlawn Drive, Honolulu, HI 96822, USA; jiayiliu@hawaii.edu
[2] Institute for Astronomy, University of Hawai'i at Mānoa, 34 Ohia Ku Street, Pukalani, HI 96768, USA
[3] Heliophysics Science Division, NASA Goddard Space Flight Center, 8800 Greenbelt Road, Greenbelt, MD 20771, USA
[4] National Solar Observatory, 22 Ohia Ku Street, Pukalani, HI 96768, USA
Received 2024 September 7; revised 2024 November 7; accepted 2024 November 26; published 2025 January 22

Abstract

Quiet-Sun regions cover most of the Sun's surface; their magnetic fields contribute significantly to solar chromospheric and coronal heating. However, characterizing the magnetic fields of the quiet Sun is challenging due to their weak polarization signal. The 4 m Daniel K. Inouye Solar Telescope (DKIST) is expected to improve our understanding of quiet-Sun magnetism. In this paper, we assess the diagnostic capability of the Diffraction Limited Near Infrared Spectropolarimeter (DL-NIRSP) instrument on DKIST for the energy transport processes in the quiet-Sun photosphere. To this end, we synthesize high-resolution, high-cadence Stokes profiles of the Fe I 630 nm lines using a realistic magnetohydrodynamic simulation, degrade them to emulate the DKIST/DL-NIRSP observations, and subsequently infer the vector magnetic and velocity fields. For the assessment, we first verify that a widely used flow tracking algorithm, the Differential Affine Velocity Estimator for Vector Magnetograms, works well for estimating the large-scale (>200 km) photospheric velocity fields with these high-resolution data. We then examine how the accuracy of the inferred velocity depends on the temporal resolution. Finally, we investigate the reliability of the Poynting flux estimate and its dependence on the model assumptions. The results suggest that the unsigned Poynting flux, estimated with existing schemes, can account for about 71.4% and 52.6% of the reference ground truth at $\log\tau = 0.0$ and $\log\tau = -1$. However, the net Poynting flux tends to be significantly underestimated. The error mainly arises from the underestimated contribution of the horizontal motion. We discuss the implications for DKIST observations.

Unified Astronomy Thesaurus concepts: Quiet Sun (1322); The Sun (1693); Solar physics (1476); Solar photosphere (1518); Solar magnetic fields (1503); Spectropolarimetry (1973)

1. Introduction

The quiet Sun refers to the region outside the sunspots and active regions, which occupies most of the solar surface at all times. The magnetic fields are organized as a complex network entrained between the convective cells. While the mean magnetic flux density is low, the total unsigned magnetic flux is comparable to that of the active regions, and the flux emergence rate is larger than that of the active regions (M. Goic et al. 2014, 2016).

The quiet-Sun magnetic fields provide important contributions to the energy budget in the solar atmosphere. New and existing magnetic fields frequently interact with each other and with convective flows, which can lead to ubiquitous nanoflares and magnetohydrodynamic (MHD) waves (D. B. Jess et al. 2023). MHD simulations of the quiet Sun suggest that these interactions can provide enough energy to heat the chromosphere and corona (M. Rempel 2014; A. J. Finley et al. 2022). Recent observations from Solar Orbiter (D. Berghmans & D. M. Long 2021) indicate that the solar atmosphere above the quiet Sun is in fact very dynamic at small scales.

Since the discovery of sunspot magnetic fields (G. E. Hale 1908), a lot of effort has been made to extract information from the solar spectra, for example, by inverting the radiative transfer equation (J. C. del Toro Iniesta & B. Ruiz Cobo 2016) or by using radio methods (C. E. Alissandrakis & D. E. Gary 2021). Spectropolarimetry, which measures the wavelength-dependent Stokes parameters (I, Q, U, V) in magnetically sensitive spectral lines, is one of the most powerful methods of diagnosing the solar magnetic field. The shape of Stokes profiles contains information about temperature, the magnetic field, and other MHD state variables of the solar atmosphere. These parameters can be inferred by solving the polarized radiative transfer equations, a process known as "inversion."

The quiet-Sun magnetic fields are challenging to infer because of their relatively low mean flux density and thus their weak polarization signal (L. Bellot Rubio & D. Orozco Suárez 2019). The study of quiet-Sun energy transport is further limited by the spatial and temporal resolution of observations. According to MHD simulations of the quiet Sun, 50% of the energy resides on a scale smaller than 100 km. A sampling rate of 8 km or smaller is needed to properly recover the spectral energy distribution (M. Rempel 2014), which requires a 10 m class telescope aperture at the optical wavelengths. For the typical quiet Sun, slit-based spectrographs often require long integration time and thus tens of minutes to assemble a raster. The average lifetime of internetwork magnetic elements, however, is only about 10 minutes (A. G. de Wijn et al. 2008; G. P. Zhou et al. 2010). The quiet-Sun magnetic fields will have significantly evolved during the scan.

Despite these difficulties, efforts have been made in estimating the energy flux through the quiet-Sun photosphere. Using observations from the Hinode satellite, F. Giannattasio et al. (2020) studied the supergranular spatial and temporal

[5] DKIST Ambassador.

scales and found that the energy flux is sufficient in sustaining the magnetic fields in the network. In contrast, D. Tilipman et al. (2023) found the energy flux inferred from the SUNRISE mission data hardly matches the radiative loss of the solar corona at the granular scales.

The 4 m Daniel K. Inouye Solar Telescope (DKIST; T. R. Rimmele et al. 2020) is expected to improve our understanding of small-scale magnetism and energy transport via its high-resolution spectropolarimetric observations (M. P. Rast et al. 2021). The Diffraction Limited Near Infrared Spectropolarimeter (DL-NIRSP; S. A. Jaeggli et al. 2022), one of the first-light instruments of DKIST, can measure Stokes parameters at an effective resolution of 0.″03 (∼22 km) with high spectral resolution and polarimetric accuracy. Using an integral field unit, it can obtain spectropolarimetric information of a 2D field of view (FOV) at the same time, at a fast cadence of several seconds.

In this paper, we will investigate how well DL-NIRSP observations can characterize the energy transport in the quiet Sun. We will use a realistic MHD simulation to create synthetic DL-NIRSP observations for the solar photosphere. Subsequently, we will use an inversion algorithm to infer the depth-dependent vector magnetic fields, and finally use these magnetic maps to estimate the velocity fields and the Poynting flux. The derived quantities will be compared with the MHD ground truth.

The rest of the paper is organized as follows. In Section 2, we describe the MHD model, the Stokes synthesis and inversion algorithm, and the flow tracking algorithm for velocity estimation. In Section 3, we focus on validating the flow tracking method on high-resolution data. In Section 4, we present the results of estimating energy transport from the emulated observation data. In Section 5, we discuss our results and analyze the possible causes for discrepancies. In Section 6, we draw our conclusions.

2. Data and Method

2.1. MHD Simulation

To simulate DL-NIRSP's high-resolution observations, we use the MPS/University of Chicago Radiative MHD (MURaM; A. Vögler et al. 2005) simulation, which is widely used in solar dynamo studies. The MURaM code solves realistic equations of state with partial ionization and radiative transfer in 3D to simulate relevant atmospheric parameters. The simulations can produce small-scale magnetic features that well resemble high-resolution observations of the solar photosphere (S. Danilovic et al. 2010). The model atmospheres are calculated in a Cartesian coordinate frame.

The model used here is from the quiet-Sun magnetoconvection run `O16bM` from M. Rempel (2014). It is initialized with a distribution of mixed-polarity fields with an average magnetic flux density of $\langle B \rangle \sim 120$ G at $\log \tau_{500} = 0$, where τ_{500} represents the optical depth at continuum wavelength 500 nm. Hereafter we use τ to represent τ_{500}. The computation box contains 1536 × 1536 × 128 pixels with a pixel size of 16 km in the horizontal direction and 12 km in the vertical direction. The temporal step is 2 s. These high-resolution simulations have also been used to understand the instrument influences for Hinode/Spectropolarimeter (M. van Noort 2012) and SUNRISE/IMaX (D. Orozco Suárez et al. 2010).

In this paper, we analyze the MURaM simulation with a cadence of $\Delta t = 2$ s, which is the highest cadence made available to us. We choose a region of interest of 512 × 512 × 128 pixels from the center of the simulation box. For each frame, we make use of the following MHD variables: temperature T, gas density ρ, gas pressure P_g, electron pressure P_e, vector velocity field $\boldsymbol{v}$, and vector magnetic field $\boldsymbol{B}$. Examples of the temperature, vertical field B_z, and vertical velocity v_z maps at $t = 2$ s at $\log \tau = 0.0$ and -1.0 are shown in Figure 1. Vigorous convective patterns are more pronounced at $\log \tau = 0$ compared to $\log \tau = -1$. The rms magnetic field ($B_{\rm rms}$) is 198.4 G at $\log \tau = 0$ compared to the $B_{\rm rms}$ equal to 129.3 G at $\log \tau = -1$.

2.2. Stokes Synthesis and Inversion

Many inversion methods have been developed to extract information from Stokes observations (J. C. del Toro Iniesta & B. Ruiz Cobo 2016). One widely used algorithm is Stokes Inversion Based on Response Functions (SIR; B. Ruiz Cobo & J. C. del Toro Iniesta 1992), which is capable of inferring depth-dependent physical properties from multiple spectral lines. Given a set of MHD state variables along the line of sight (LOS), SIR can also forward-model the emergent Stokes profiles. SIR operates under the assumption of hydrostatic equilibrium and local thermodynamic equilibrium (LTE).

In the synthesis mode, SIR numerically solves the polarized radiative transfer equation in magnetically sensitive lines:

$$\frac{d\boldsymbol{I}(\tau)}{d\tau} = K(\tau)[\boldsymbol{I}(\tau) - \boldsymbol{S}(\tau)], \tag{1}$$

where $\boldsymbol{I} = (I, Q, U, V)$ is the Stokes vector with a polarization signal induced by the Zeeman effect, K is the total absorption matrix, $\boldsymbol{S} = (S_I, S_Q, S_U, S_V) = (B_\nu(T), 0, 0, 0)$ is the source function vector, and $B_\nu(T)$ is the Planck function. Here K and $\boldsymbol{S}$ are evaluated under the assumption of LTE. To simplify the problem, we synthesize four Stokes profiles only at the disk center with a spectral sampling rate of 8.95 mÅ over a spectral window of 2.459 Å, which covers −655.9 to 1803.9 mÅ from the rest wavelength of the line core of Fe I at 630.15 nm. These parameters are typical for DKIST/DL-NIRSP observations. Furthermore, we convolve the synthesized spectra with the theoretical point-spread function (PSF) of DKIST/DL-NIRSP and resample the pixel size to 0.″03 (about 22 km) to emulate a DL-NIRSP observation using High-Res mode (f/62), which has a resolution at the diffraction limit (0.″03; S. A. Jaeggli et al. 2022). We do not add noise to the synthetic spectra for this study. The effect of noise can be important (e.g., C. Quintero Noda et al. 2023); however we will defer its investigation to future work.

In the inversion mode, SIR modifies the initial model atmosphere iteratively until the synthetic Stokes profiles match the observed ones. It returns the τ-dependent temperature, LOS velocity, magnetic field strength, inclination, and azimuth angles along the LOS. The fitting is performed by introducing perturbations to the initial guess of the atmosphere, and minimizing the χ^2 between the observed and modeled Stokes profiles:

$$\chi^2 = \frac{1}{\nu}\sum_{k=1}^{4}\sum_{i=1}^{M}[I_k^{\rm obs}(\lambda_i) - I_k^{\rm syn}(\lambda_i)]^2\frac{\omega_k^2}{\sigma_k^2}, \tag{2}$$

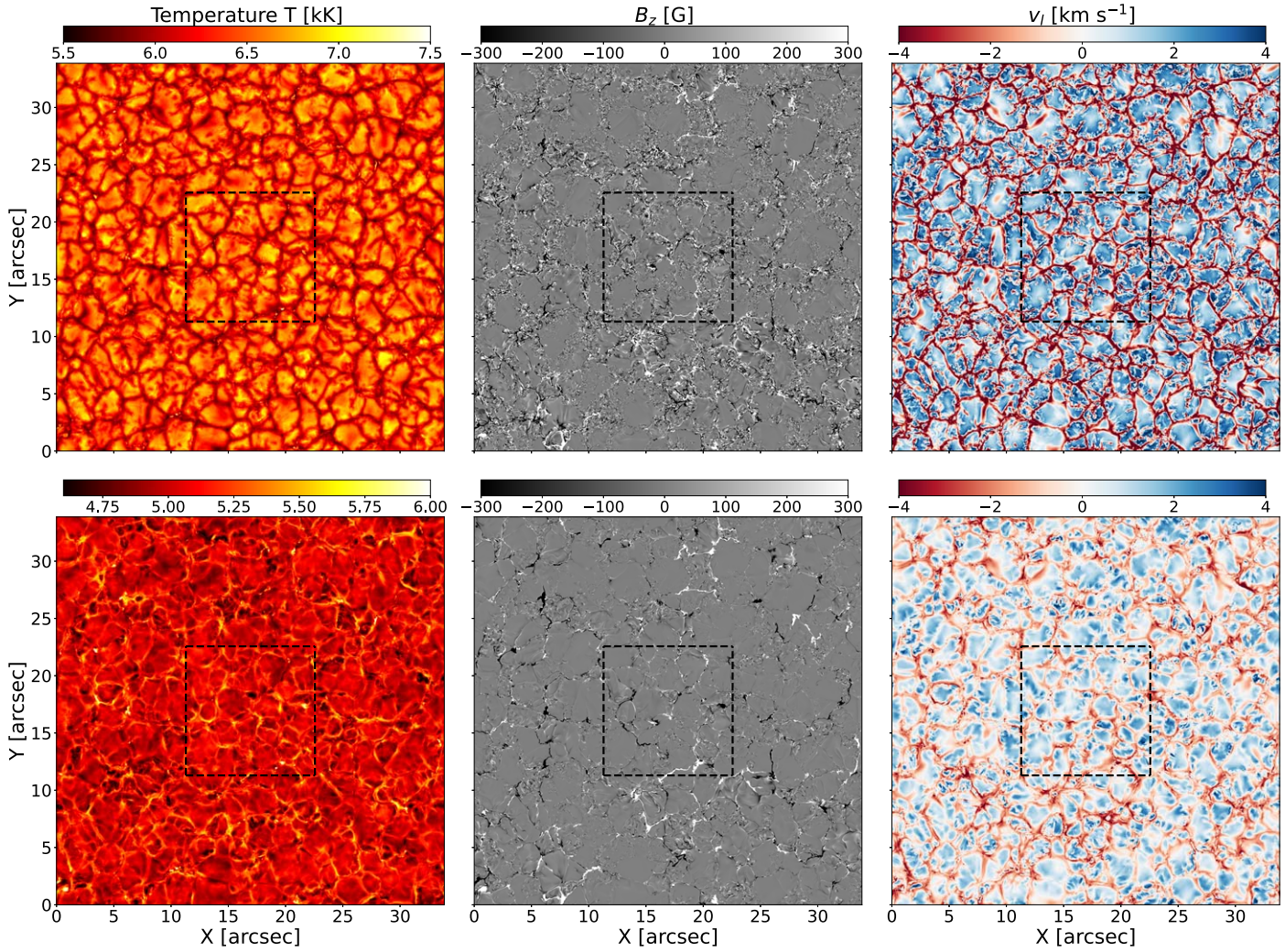

Figure 1. Overview of MURaM simulation at $\log\tau = 0$ (top) and $\log\tau = -1$ (bottom) at $t = 2$ s. From left to right, the maps are for the temperature T, vertical magnetic field B_z, and vertical velocity v_l. The black dashed box marks the region of interest in this work.

where ν is the number of free parameters, k is the index of the four Stokes parameters, i is the index of the wavelength points, and ω_k and σ_k are the weights and uncertainties for each Stokes parameter. In order to reduce the number of free parameters, the parameters are evaluated only at several "nodes," i.e., grid points with fixed τ, and the values at the remaining τ grid points are approximated by interpolation. To extract the information from degraded Stokes profiles, we invert the spectra with the node configuration listed in Table 1 (C. Quintero Noda et al. 2023). The weights for Stokes (I, Q, U, V) in chi-square evaluation are (2, 20, 20, 5), respectively.

We note that the inferred variables are typically a function of τ. A 2D map generally represents a slice with constant τ with varying geometric height z. Such is the limitation of many inversion algorithms (including SIR), which assume hydrostatic equilibrium and lack an absolute height scale along the LOS (A. Pastor Yabar et al. 2019).

2.3. Resolving 180° Azimuthal Ambiguity

For the Zeeman effect, magnetic fields with azimuths differing by 180° produce exactly the same linear polarization state. Additional assumptions are required to resolve this ambiguity (T. R. Metcalf et al. 2006; K. D. Leka et al. 2009). One widely used algorithm is the minimum energy method (T. R. Metcalf 1994). It disambiguates the magnetic field by minimizing the summed absolute divergence of the magnetic field and the vertical electric current density:

$$E = \sum |\nabla \cdot \boldsymbol{B}| + \lambda \sum |J_z| \tag{3}$$

where λ is a weighting factor that controls the relative importance of the vertical electric current density. The vertical derivative in the divergence of the magnetic field is obtained

Table 1
Summary of SIR Algorithm Configuration

	Nodes			
Parameters	Cycle 1	Cycle 2	Cycle 3	Cycle 4
Temperature	2	3	5	5
Microturbulence	1	1	1	1
LOS velocity	1	2	3	5
Magnetic field strength	1	2	3	5
Inclination	1	2	3	5
Azimuth	1	2	2	2

from a potential field calculated directly from the vertical magnetic field B_z.

In our study, we apply this algorithm to the magnetic fields inverted by SIR at $\log\tau = 0$ and $\log\tau = -1.0$, assuming the $\boldsymbol{B}$ vectors fall on a geometric height. As we shall see, the assumption is not strictly valid, but is a necessary simplifying step. We set $\lambda = 0.5$ as it gives a smooth solution.

2.4. Velocity Fields and Poynting Flux Estimate

The temporal change of magnetic energy E_m in a solar atmospheric volume V with boundary S can be calculated with an equation that involves the electric field $\boldsymbol{E}$, magnetic field $\boldsymbol{B}$, current density $\boldsymbol{J}$, and velocity field $\boldsymbol{v}$:

$$\frac{dE_m}{dt} = \frac{1}{4\pi}\oint_S \boldsymbol{E}\times\boldsymbol{B}\cdot\boldsymbol{n}\,dS - \frac{1}{c}\int_V \boldsymbol{v}\cdot(\boldsymbol{J}\times\boldsymbol{B})\,dV, \quad (4)$$

where $\boldsymbol{n}$ is the normal unit vector of the boundary. The first term on the right-hand side is the vertical Poynting flux (S_z), which measures the flow of electromagnetic energy through the boundary. In practice, we only consider the Poynting flux through the bottom boundary, which is usually the photosphere. The second term on the right-hand side is the power of the work done by the Lorentz force, which converts kinetic energy to magnetic energy. The second term is usually ignored under the force-free condition. We will examine this approach in Section 5.3.

The electric field $\boldsymbol{E}$ may be measured via the Stark effect or may be estimated by using the ideal Ohm's law ($\boldsymbol{E} = -\boldsymbol{v}\times\boldsymbol{B}$). The former method has been recognized to be critically affected by the low sensitivity of observations (T. Moran & P. Foukal 1991). The latter method requires knowledge of the full vector velocity field. While the LOS velocity v_l can be directly estimated from the Doppler effect, the full vector velocity field $\boldsymbol{v}$ needs to be estimated from flow tracking methods (e.g., B. T. Welsch et al. 2007; P. W. Schuck 2008). For example, the velocity can be inferred by taking advantage of the physical relation between $\boldsymbol{v}$ and $\boldsymbol{B}$ via the induction equation (e.g., K. Kusano et al. 2002; D. W. Longcope 2004; B. T. Welsch et al. 2004; P. W. Schuck 2006, 2008), in particular the normal component of its ideal version:

$$\frac{\partial B_z}{\partial t} = -\nabla_h\cdot(B_z\boldsymbol{v}_h - \boldsymbol{B}_h v_z), \quad (5)$$

where the subscript h denotes the horizontal component that is parallel to the photosphere. Given a time sequence of $\boldsymbol{B}$ maps, one may infer the velocity fields $\boldsymbol{v}$ using Equation (5). The problem is generally not well posed and requires additional constraints.

The Differential Affine Velocity Estimator for Vector Magnetograms (DAVE4VM; P. W. Schuck 2008) is a widely used, local flow tracking method. It estimates the plasma velocities by minimizing the L2 norm of the residual (difference of the left- and right-hand sides) of Equation (5) within a windowed subregion. Recently, the algorithm has been modified to include the observed Doppler velocity v_l as an additional constraint. Termed DAVE4VMwDV (with Doppler Velocity; P. W. Schuck 2025, in preparation), the global loss function L now reads

$$\begin{aligned} L &= L_1 + \lambda L_2,\\ L_1 &= \sum_w \left\{\frac{\partial B_z}{\partial t} + \boldsymbol{\nabla}_h\cdot(B_z\boldsymbol{v}_h - \boldsymbol{B}_h v_z)\right\}^2 \sigma^{-2}_{\partial_t B_z},\\ L_2 &= \sum_w (\hat{\boldsymbol{\eta}}\cdot\boldsymbol{v} - v_l)^2\sigma^{-2}_{v_l}, \end{aligned} \quad (6)$$

where $\boldsymbol{B}$ and v_l are the observational input, and $\boldsymbol{v}$ is the output. Here λ is a scalar multiplier that controls the importance of the L_2 term, the subscript w denotes the window, σ_X refers to the uncertainty of variable X ($\partial_t B_z$ or v_l), and the unit vector $\hat{\boldsymbol{\eta}}$ specifies the LOS direction. The operator $\boldsymbol{\nabla}_h$ acts on the horizontal components alone. In practice, we use a three-point stencil to calculate the time derivative, and a five-point stencil for the spatial derivatives, specifically

$$\left.\frac{\partial f}{\partial t}\right|_{t=t_0} = \frac{f(t_0+\Delta t) - f(t_0-\Delta t)}{2\Delta t}, \quad (7)$$

where we quote Δt as the cadence of the output. We opt for this numerical scheme so that the inferred velocity can be cotemporal with the magnetogram: both are needed for the Poynting flux estimate. Appendix B provides some discussion on this choice.

The algorithm requires several free parameters: the degree of Legendre expansion for horizontal velocity d and vertical velocity d_r, the window size w, and the relative weighting factor λ. These parameters can be empirically optimized to reduce L.

The inferred vector velocity field from DAVE4VMwDV then allows us to estimate the vertical Poynting flux S_z passing through the photosphere via a surface integral:

$$\begin{aligned} S_z &= S_z^{\rm em} + S_z^{\rm sh}\\ &= \frac{1}{4\pi}\int_S B_h^2 v_z\,dS - \frac{1}{4\pi}\int_S (\boldsymbol{B}_h\cdot\boldsymbol{v}_h)B_z\,dS. \end{aligned} \quad (8)$$

Here the Poynting flux is typically divided into two terms. The emerging term $S_z^{\rm em}$ corresponds to the first integral, which measures the energy transport due to the emergence (vertical transport) of magnetic flux tubes. The shearing term $S_z^{\rm sh}$ corresponds to the second integral, which measures the energy transport resulting from the horizontal flow that shears the magnetic field.

3. DAVE4VMwDV on Simulation Data

The DAVE4VM algorithm was originally tested on an MHD simulation with a 348 km grid size (P. W. Schuck 2008). It has been applied widely on existing, low-resolution magnetograms with $\sim 1''$ resolution ($\sim$720 km), and mostly on active regions with stronger magnetic fields. Its performance in high-resolution, quiet-Sun regions has not been demonstrated.

3.1. Performance of DAVE4VMwDV at Different Optical Depths

In this section, we investigate the performance of DAVE4VMwDV at different optical depths, similar to the analysis on real data. Hereafter we choose to focus on two layers, $\log\tau = 0$ and $\log\tau = -1$, because these two layers roughly bracket the range of formation height for the Fe I

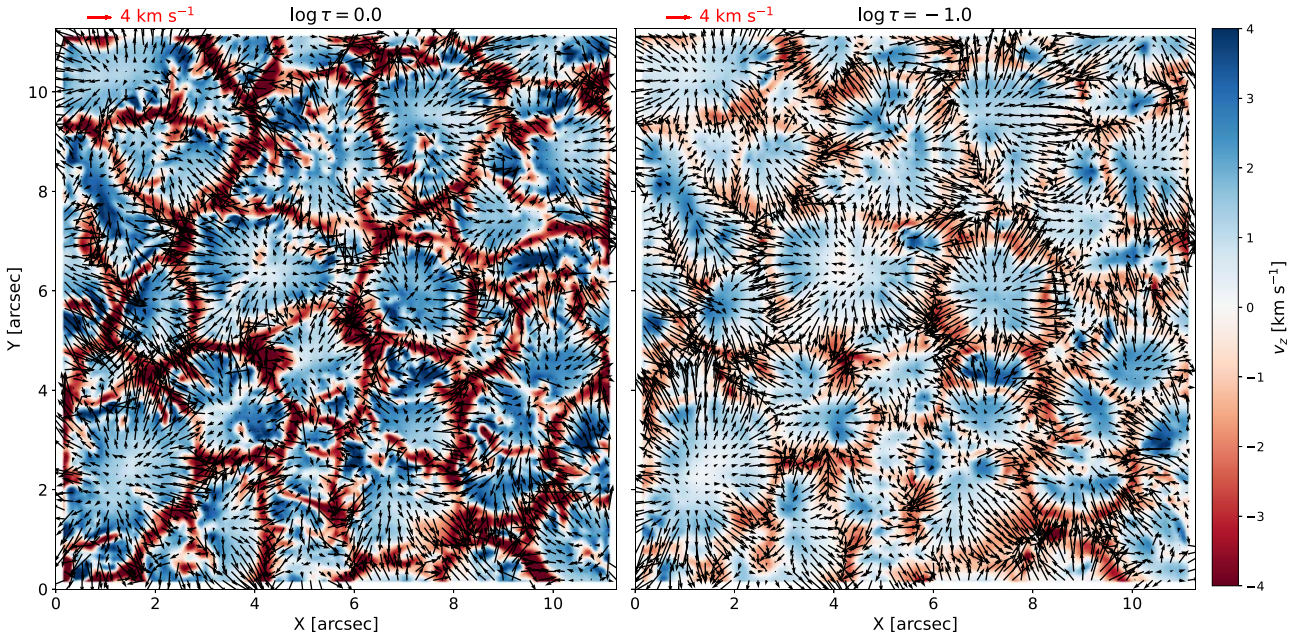

Figure 2. The inferred velocity field at $\log\tau = 0$ (left) and $\log\tau = -1$ (right) with input temporal resolution of $\Delta t = 2$ s. The horizontal arrows indicate the direction and amplitude of the horizontal velocity. The vertical velocities are plotted as the background.

630 nm lines. These two layers correspond to the height of approximately $h = 0$ km and $h = 135$ km above the photosphere according to the widely adopted solar atmospheric model FALC (J. M. Fontenla et al. 2006). To extract the maps from the MURaM simulation, we interpolate the magnetic and velocity fields to the τ space.

To quantify the overall performance, we evaluate the Pearson and Spearman correlation coefficients between all three components of the inferred velocity ($\boldsymbol{v}_{\rm DV}$) and the MURaM ground-truth velocity ($\boldsymbol{v}_{\rm GT}$). We further consider three other metrics following the analyses in C. J. Schrijver et al. (2006) and B. Tremblay & R. Attie (2020): the spatially averaged relative error

$$E_{\rm rel}[\boldsymbol{v}_{\rm DV}, \boldsymbol{v}_{\rm GT}] = \left\langle \sqrt{\frac{(\boldsymbol{v}_{\rm DV} - \boldsymbol{v}_{\rm GT})^2}{\boldsymbol{v}_{\rm DV} \cdot \boldsymbol{v}_{\rm GT}}} \right\rangle, \tag{9}$$

the vector correlation coefficient

$$C[\boldsymbol{v}_{\rm DV}, \boldsymbol{v}_{\rm GT}] = \frac{\langle \boldsymbol{v}_{\rm DV} \cdot \boldsymbol{v}_{\rm GT} \rangle}{\langle \|\boldsymbol{v}_{\rm DV}\|_2 \rangle \langle \|\boldsymbol{v}_{\rm GT}\|_2 \rangle}, \tag{10}$$

and the cosine similarity index, which measures the average cosine of the angle between the ground-truth velocity and inferred velocity

$$A[\boldsymbol{v}_{\rm DV}, \boldsymbol{v}_{\rm GT}] = \left\langle \frac{\boldsymbol{v}_{\rm DV} \cdot \boldsymbol{v}_{\rm GT}}{\|\boldsymbol{v}_{\rm DV}\|_2 \|\boldsymbol{v}_{\rm GT}\|_2} \right\rangle. \tag{11}$$

The perfect inferred velocities should have $E_{\rm rel} = 0$, $C = 1.0$, and $A = 1.0$.

In this test, we use the vector magnetic fields and Doppler velocity at $t = 2$ s as input for each optical depth. The time derivative of $\partial B_z/\partial t$ at $t = 2$ s is calculated from B_z at $t = 0$ s and $t = 4$ s. The uncertainties for $\partial B_z/\partial t$ are set as the difference between $\partial B_z/\partial t$ and the ideal induction equation (nonideal effects owing to, e.g., intrinsic numerical errors of the simulation or spatial/spectral binning), and the uncertainty for v_l is taken to be a typical observational value 200 m s^{-1}. For the DAVE4VMwDV free parameters, we set the window size to $w = 15$, and the degree of Legendre expansion in the horizontal and vertical directions is $d = 5$ and $d_r = 7$ for $\log\tau = 0.0$ and $d = 3$ and $d_r = 5$ for $\log\tau = -1.0$, respectively. The choice of free parameters is discussed in Appendix A.1.

The maps of the inferred velocity field are shown in Figure 2. Both layers show the expected convective flow pattern: diverging in the granular cell centers and converging in the intergranular lanes. The inferred velocities are generally smoother than the ground-truth velocities (see Figure 1). Some fine structures, in particular narrow downflow lanes extending from the intergranular lane to the granular cell center, are not well reproduced.

The scatter plots between the inferred and the ground-truth velocities at the two optical depths are shown in Figure 3. The inferred velocity at $\log\tau = 0$ has $E_{\rm rel} = 0.28$, $C = 0.95$, and $A = 0.95$, while the inferred velocity at $\log\tau = -1$ has $E_{\rm rel} = 0.23$, $C = 0.97$, and $A = 0.96$. It appears that DAVE4VMwDV has better performance on the higher layer, which has less vigorous convection and thus less complex spatial structure.

Despite all three components of the inferred velocities having Pearson/Spearman coefficients greater than 0.9 at both layers, the slopes between the inferred velocities and ground-truth velocities are smaller than 1, suggesting an overall underestimation of the flow fields. The mean magnitudes of the inferred velocity $v = \sqrt{v_x^2 + v_y^2 + v_z^2}$ at $\log\tau = 0$ and $\log\tau = -1$ are 3.4 km s^{-1} and 2.9 km s^{-1}, respectively, compared to 3.8 km s^{-1} and 3.1 km s^{-1} from the ground truth.

3.2. The Effect of Temporal Resolution on Velocity Estimates

We apply DAVE4VMwDV on MURaM data with five different cadences to investigate the effect of temporal

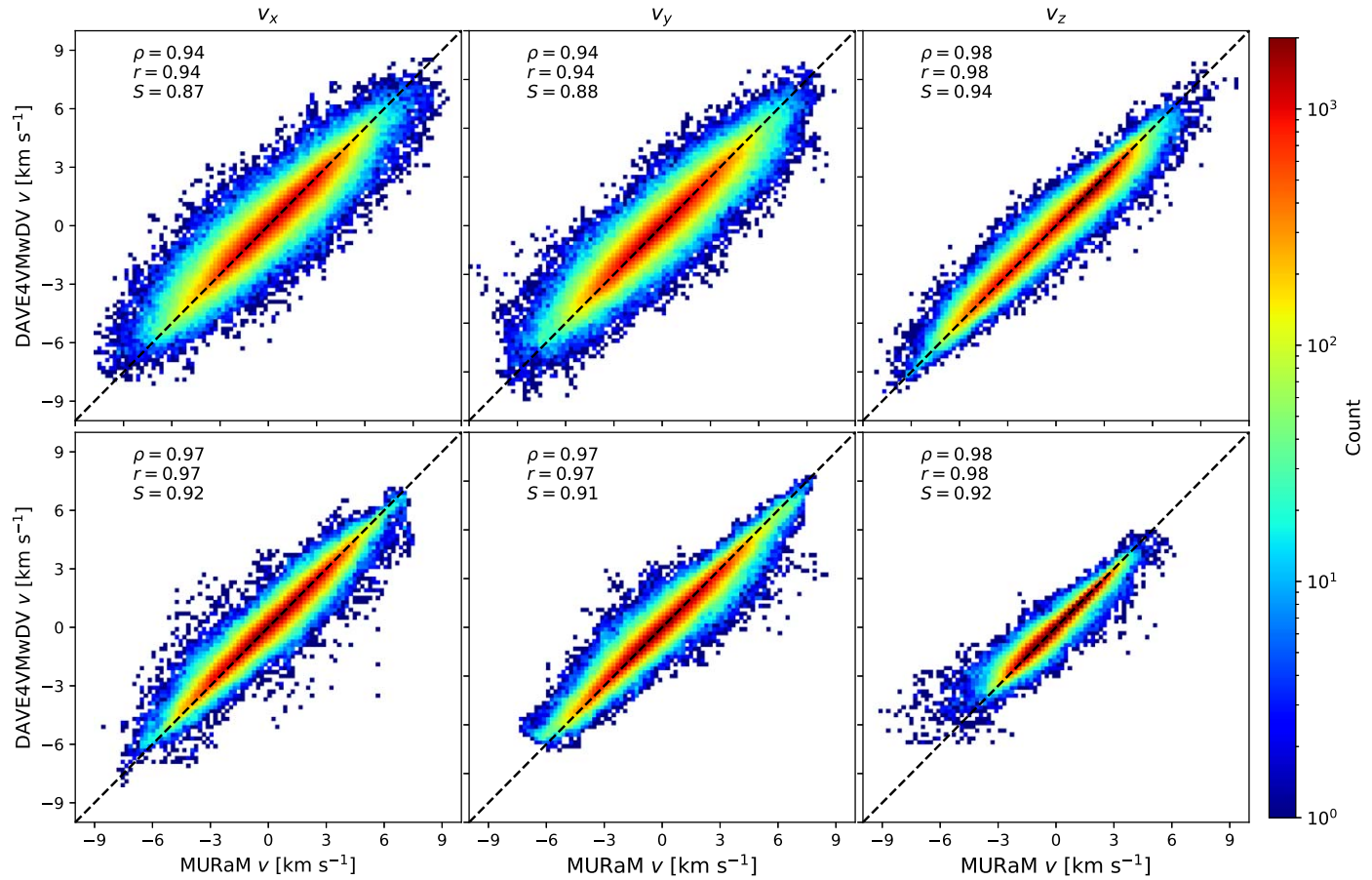

Figure 3. 2D histograms of the inferred velocity field and the reference velocity field at $\log\tau = 0$ (top) and $\log\tau = -1$ (bottom). From left to right, we show the histograms for v_x, v_y, and v_z. The Spearman coefficient (ρ), Pearson coefficient (r), and slope (S) are also shown on the plots.

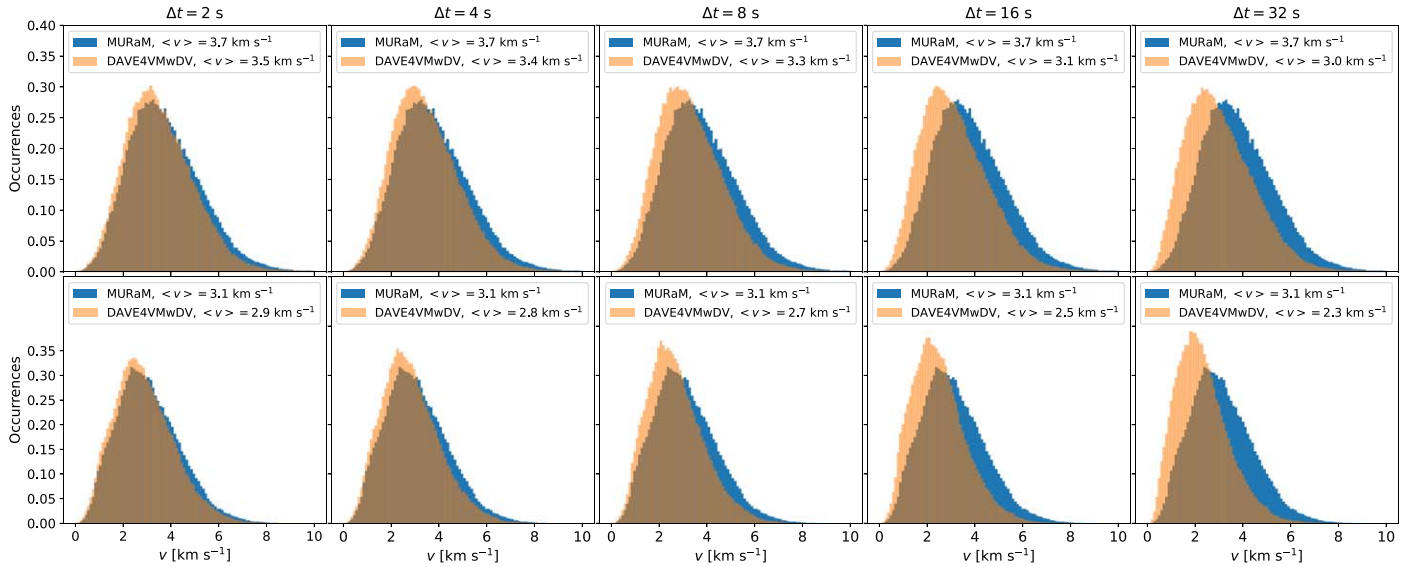

Figure 4. Histograms of the magnitude of the ground-truth velocity (blue) and inferred velocity (orange) from magnetograms with different temporal resolution. Top: histograms for $\log\tau = 0$. Bottom: histograms for $\log\tau = -1$. From left to right, we show the results with $\Delta t = [2, 4, 8, 16, 32]$ s.

resolution. The input parameters are the magnetograms and Dopplergram at $t_0 = 32$ s at $\log\tau = 0$ and $\log\tau = -1$. The time derivatives of the vertical magnetic field are calculated from the vertical magnetic fields at $t_1 = [30, 28, 24, 16, 0]$ s and $t_2 = [34, 36, 40, 48, 64]$ s, so that the nominal cadences are $\Delta t = [2, 4, 8, 16, 32]$ s.

The histograms of the velocity magnitudes inferred with the various cadences are shown in Figure 4. The overall magnitude is always smaller than the ground truth, even in the case of the highest cadence. As the cadence decreases (greater Δt), the distribution of the inferred velocity magnitude becomes narrower, and deviates more from the ground truth for both

Table 2
Summary of Estimated Poynting Flux

Optical Depth	Source	$\langle S_z \rangle$	$\langle \lvert S_z \rvert \rangle$	$\langle S_z^{\rm em} \rangle$	$\langle S_z^{\rm sh} \rangle$	$\langle \lvert S_z^{\rm sh} \rvert \rangle$
$\log\tau = 0.0$	MURaM, Ground Truth	3.7	278.9	−68.4	72.1	201.1
	MURaM, DAVE4VMwDV	−16.2	269.4	−68.1	51.9	175.5
	Emulation, DAVE4VMwDV	−10.5	150.5	−23.0	12.5	95.2
$\log\tau = -1.0$	MURaM, Ground Truth	30.2	75.7	−27.8	58.0	75.3
	MURaM, DAVE4VMwDV	7.4	64.0	−24.7	32.2	53.6
	Emulation, DAVE4VMwDV	−8.6	36.2	−13.7	5.1	22.7

Note. The unit for all values is 10^6 erg cm^{-2} s^{-1}. The quantities from left to right are the net Poynting flux $\langle S_z \rangle$, average unsigned Poynting flux $\langle \lvert S_z \rvert \rangle$, average emergence term of Poynting flux $\langle S_z^{\rm em} \rangle$, average shearing term of Poynting flux $\langle S_z^{\rm sh} \rangle$, and average unsigned shearing term of Poynting flux $\langle \lvert S_z^{\rm sh} \rvert \rangle$.

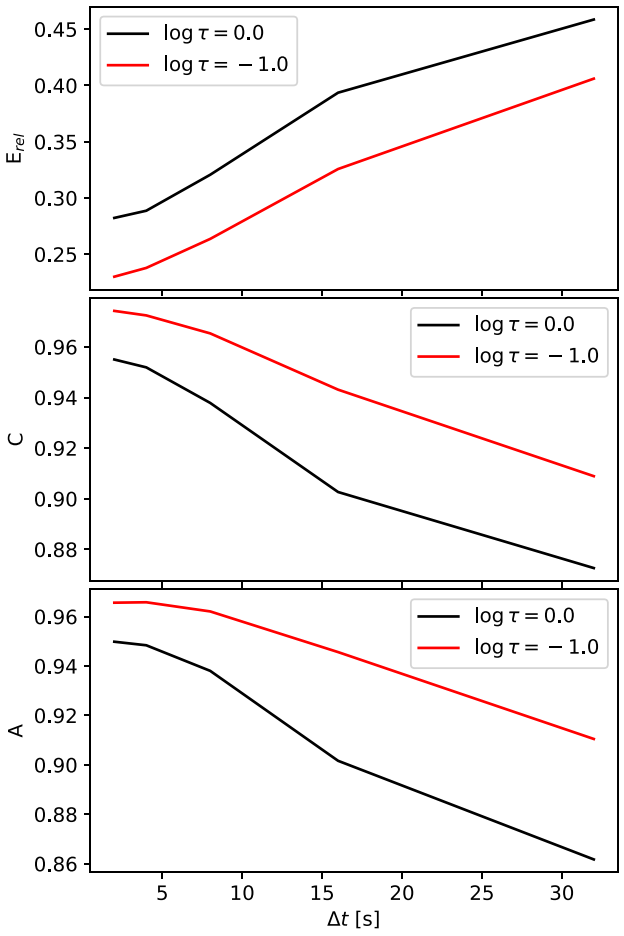

Figure 5. Variation of metrics $E_{\rm rel}$, C, and A (from top to bottom) with respect to cadence Δt. The black lines represent the metrics at $\log\tau = 0.0$, and the red lines represent the metrics at $\log\tau = -1.0$.

layers. In the case with $\Delta t = 32$ s, the average velocity magnitude decreases to 3.0 km s^{-1} and 2.3 km s^{-1} at $\log\tau = 0$ and $\log\tau = -1$, compared to the ground-truth values of 3.7 km s^{-1} and 3.1 km s^{-1}.

Figure 5 shows the performance metrics $E_{\rm rel}$, C, and A for the velocity at $\log\tau = 0$ (black) and $\log\tau = -1$ (red). The model performance is consistently better at the higher layer as previously mentioned. As Δt increases, all three metrics become worse. We posit that the worsening performance after $\Delta t \geqslant 4$ s may be attributed to the violation of the Courant–Friedrichs–Lewy (CFL) condition. The average horizontal velocities are $v_h = 2.9$ km s^{-1} and 2.8 km s^{-1} at $\log\tau = 0$ and -1, respectively. For the MURaM horizontal grid size of 16 km, a cadence of $\Delta t = 2.5$ s or better is required.

3.3. Estimation of Poynting Flux

Based on the velocity inferred by DAVE4VMwDV, we may estimate the Poynting flux through the surface with Equation (8). The estimated Poynting fluxes are listed in Table 2. The ground truth and the estimated Poynting flux maps are shown in the left and middle columns of Figure 6, respectively. The inference results qualitatively recover the pattern of ground truth, with large S_z values concentrated near the intergranular lanes.

While Poynting flux of both signs exists near the intergranular lanes, there are overall more negative occurrences. In contrast, the granular cell centers have relatively uniform but weak positive Poynting flux. From $\log\tau = 0$ to -1, the fractional area occupied by large Poynting flux decreases with height, and the pattern becomes less structured, reminiscent of the flow maps.

The average unsigned Poynting flux is greater at the lower layer: the value for $\log\tau = 0$ is 2.8×10^8 erg cm^{-2} s^{-1}, while that for $\log\tau = -1$ is 0.8×10^8 erg cm^{-2} s^{-1}. Quite interestingly, the net Poynting flux is greater at the higher layer: the value for $\log\tau = 0$ is 3.7×10^6 erg cm^{-2} s^{-1}, while that for $\log\tau = -1$ is 3.0×10^7 erg cm^{-2} s^{-1}, almost an order of magnitude larger. This is because the convection is stronger in the lower layer so that the magnitude of vertical velocity is larger bringing more downward Poynting flux, which cancels out the upward Poynting flux.

We compare the inferred values to the ground truth. The estimated unsigned Poynting flux can recover 96.4% and 84.2% of the ground-truth unsigned Poynting flux at $\log\tau = 0$ and $\log\tau = -1$, respectively. However, the estimated net Poynting fluxes at these two layers are -1.6×10^7 erg cm^{-2} s^{-1} and 7.4×10^6 erg cm^{-2} s^{-1}, respectively. They are quite far from the ground truth in magnitude, and have the wrong sign for $\log\tau = 0.0$. We will discuss below the cause of the mismatch.

The last column of Figure 6 shows the 2D histograms of Poynting flux between the ground truth and our estimate. While there is overall reasonable correlation between the two variables, significant scatter is apparent for both heights. To investigate the origin of the scatter, we consider the Poynting flux in regions with $\lvert B \rvert \geqslant 3\sigma_B$ and regions with $\lvert B \rvert < 3\sigma_B$ separately, where σ_B stands for the standard deviation in the FOV. The stronger-field region represents 34.4%

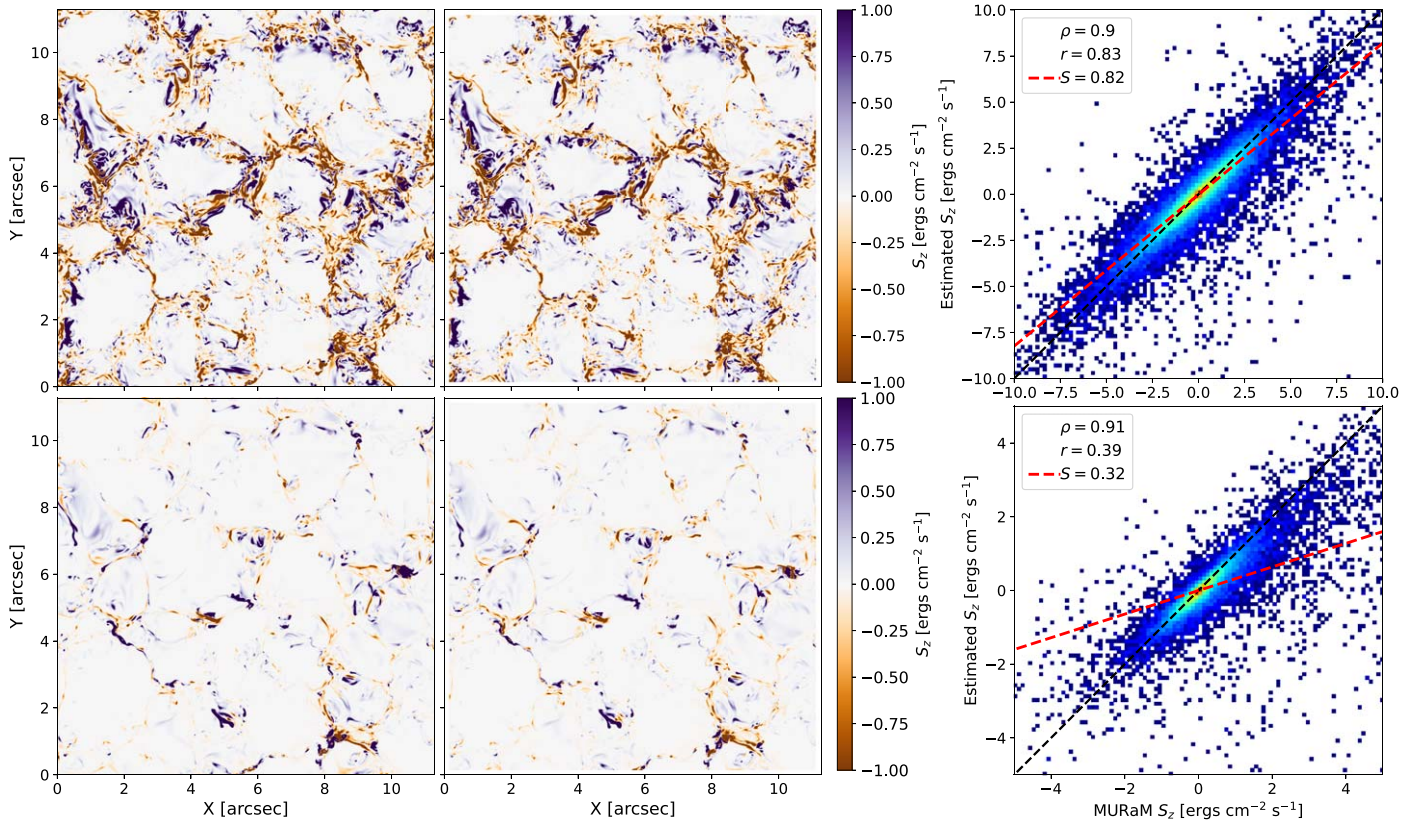

Figure 6. Comparison between Poynting flux from MHD simulation (left) and DAVE4VMwDV (middle) at $\log\tau = 0$ (top) and $\log\tau = -1$ (bottom). The right column shows the 2D histogram between the reference and estimated Poynting flux. The Spearman coefficient (ρ), Pearson coefficient (r), and linear fitting (red dashed line) between the ground truth and estimated Poynting flux are shown on the 2D histogram.

and 50.5% of the total unsigned Poynting flux at $\log\tau = 0$ and $\log\tau = -1$, respectively. In the weak-field regions, the Pearson correlation coefficients between the inferred and the ground-truth velocities are 0.91 and 0.85 for the lower and higher layers, respectively. Counterintuitively, the correlation coefficients in the stronger-field regions are only 0.78 and 0.36, suggesting that the scatter mostly results from the stronger-field pixels.

We note that a large fraction of pixels are below the one-to-one line. In weak-field regions, the net Poynting fluxes are -4.3×10^6 erg cm^{-2} s^{-1} and 6.0×10^6 erg cm^{-2} s^{-1} at the two layers, which are smaller compared to the ground-truth values of 8.6×10^5 erg cm^{-2} s^{-1} and 9.1×10^6 erg cm^{-2} s^{-1}. The Poynting flux in stronger-field regions is significantly greater and also underestimated, which accounts for the majority of the discrepancy. The net Poynting fluxes in the stronger-field regions are -3.5×10^8 erg cm^{-2} s^{-1} and 7.3×10^7 erg cm^{-2} s^{-1} at the two layers, compared to the ground-truth values of 1.3×10^8 erg cm^{-2} s^{-1} and 9.8×10^8 erg cm^{-2} s^{-1}.

We further decompose the Poynting flux into an emerging term and a shearing term. The values of these two terms are also listed in Table 2. The ground truth, net emerging term, and net shearing term have different signs at both layers. These two terms almost cancel each other out at $\log\tau = 0.0$. In contrast, the shearing term dominates the emergence term at $\log\tau = -1.0$: the absolute value is about twice as large. We find that the estimated net emerging Poynting flux can reproduce 99.6% and 88.8% of the ground truth at $\log\tau = 0$ and $\log\tau = -1$, respectively. But the estimate can only reproduce 72.0% and 55.5% of the net shearing term. The underestimation of the shearing term accounts for the majority of the mismatch of the Poynting flux.

4. Estimated Energy Transport from Emulated Observation

Above, we focused on the performance of DAVE4VMwDV on MHD simulation data. In this section, we examine the capability of estimating energy transport in the emulated DL-NIRSP observation. As we shall see, most of the conclusions in the previous section qualitatively hold.

4.1. Stokes Synthesis and MHD Variable Inference

To emulate the DL-NIRSP observation, we first synthesize the four Stokes profiles from the MURaM simulation with SIR and then degrade the profiles with the theoretical PSF of DL-NIRSP in the High-Res mode and a two-pixel binning. Figure 7 shows an example of the synthesized data in the original and degraded resolution. After degradation, the contrast in the continuum image decreases by 9%. In the Stokes V map, the original mixed-polarity features in the intergranular lane become weaker due to cancellation; lanes with stronger signals become wider.

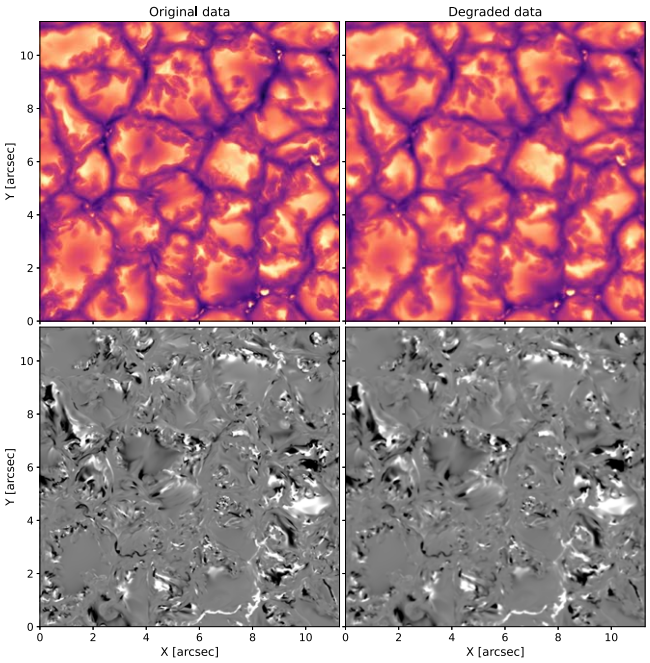

Figure 7. Original (left) and degraded (right) synthetic Stokes profiles. Upper panels show the continuum intensity I/I_c, and lower panels show the circular polarization V/I_c in the wing of the Fe I 630.15 nm line.

The comparison between the input MURaM parameters and the inferred parameters with SIR at $\log\tau = 0$ and $\log\tau = -1$ is shown in Figure 8.

At $\log\tau = 0$, the inferred temperature map and LOS velocity map have no appreciable difference from the ground-truth MURaM map. They both show typical granular structure: high temperature and upflows in granular cell centers, with low temperature and downflows in intergranular lanes. The continuum bright points in intergranular lanes are also captured. The inferred magnetic field strength shows a network-like pattern similar to the ground truth, though fine-scale structures are diminished. We will discuss below the response of the inferred magnetic field to spatial scales. The inferred inclination captures the large-scale pattern with more vertical magnetic fields filling the intergranular lanes. The small-scale mixed-polarity pattern, for example, the region centered at $(X, Y) = (3'', 3'')$ in the black dashed box, is largely missing.

At $\log\tau = -1$, the inferred temperature map appears to be overall brighter than the ground-truth map. The average inferred temperature is 5122 K, about 58 K higher than the ground truth, which is similar to findings of previous work (C. Quintero Noda et al. 2023). The difference between the inferred and ground-truth LOS velocity maps, on the other hand, appears to be minimal. The inferred magnetic field strength shows a similar pattern to ground truth, albeit one that is somewhat blurry. The average field strength in the strong-field region ($B > 100$ G) is 195 G, compared to the ground-truth value of 230 G. The inferred inclination fails to capture the small-scale mixed polarities, similar to the lower layer.

We compare the distributions of the total ($|B|$), vertical (B_z), and horizontal (B_h) magnetic fields in Figure 9. The deviation between the ground truth and the inversion results appears to be more pronounced for strong-field pixels and for the higher layer at $\log\tau = -1$. At $\log\tau = 0$, the largest deviation appears to be an underestimate of B_h for values above 500 G. For $\log\tau = -1$, the inferred fields are generally significantly weaker than the ground truth.

Inaccuracies may also originate from the azimuthal disambiguation step. Figure 10 illustrates the cosine of the azimuth ($\cos\phi$) from the MURaM model (left), versus the inferred results after the application of the ME0 algorithm (right). As evidenced by the large mismatch, the performance of the ME0 algorithm is not satisfactory. In the granular lanes, for example, in the region centered at $(X, Y) = (4'', 3'')$ in the black box, fine-scale structures where the sign of $\cos\phi$ changes within several pixels are not reproduced. The results in granular cell centers, for example, in the granular cell centered at $(X, Y) = (1''.5, 2''.5)$, where ϕ is expected to vary smoothly, are somewhat better, though patches with completely opposite signs also exist. The solution of the ME0 disambiguation algorithm is known to be unsatisfactory for the quiet Sun: similar conclusions can be found in recent work (e.g., D. Tilipman et al. 2023).

4.2. Poynting Flux from Emulated Observation

We use the inverted magnetic field and Doppler velocity maps to infer the 3D velocity field with DAVE4VMwDV. As shown in Section 3, higher cadence is preferred. To access the best performance of existing schemes, we will use the inferred vector magnetic fields and Doppler velocity at $t = 2$ s as input for each optical depth. The time derivative of $\partial B_z/\partial t$ at $t = 2$ s is calculated from B_z at $t = 0$ s and $t = 4$ s. We set window size $w = 15$ and degree of expansion $d = 3$ and $d_r = 5$ for $\log\tau = 0$, and set $w = 15$, $d = 1$, and $d_r = 5$ for $\log\tau = -1$. The choice of parameters is discussed in Appendix A. We then estimate the Poynting flux with the inferred velocity and Equation (8).

The velocity fields inferred from the emulated magnetograms are shown in Figure 11. Similar to the results for the velocity inferred from the ground-truth magnetograms in the previous section, convective patterns are well recovered for both layers. The flow direction in the granular cell center, on the other hand, appears to be more random and disordered, unlike the consistent diverging flows seen previously. Compared to the distribution of the ground-truth velocity, the inferred velocities at both layers have a narrower distribution and smaller magnitude. The average magnitude of the inferred velocity is $2.6\,\mathrm{km\,s^{-1}}$ and $2.2\,\mathrm{km\,s^{-1}}$ at $\log\tau = 0.0$ and $\log\tau = -1.0$, respectively, compared to $3.8\,\mathrm{km\,s^{-1}}$ and $3.1\,\mathrm{km\,s^{-1}}$ from the ground truth.

The estimated Poynting fluxes from emulated magnetograms at the two layers are listed in Table 2. Below, we examine the estimated emergence term (S_z^{em}) and shearing term of the Poynting flux (S_z^{sh}) separately as they are differently affected by the azimuth disambiguation procedure. The emergence term is only related to the square of the horizontal magnetic field (B_h^2), so it is not affected by the ambiguity resolution. The shearing term, on the other hand, relates to the vector horizontal magnetic field by $\boldsymbol{v}_h \cdot \boldsymbol{B}_h$, and can change the sign if the azimuth has the wrong sign. We also examine the unsigned shearing term of the Poynting flux ($\lfloor S_z^{\mathrm{sh}} \rfloor$) for completeness. The estimates of these three quantities and their comparison with the ground truth are shown in Figures 12 and 13.

At $\log\tau = 0$, the estimated emergence term captures the main features that it is negative in the intergranular lane and positive in the granular cell, though many fine-scale structures do not exhibit this. For the estimated shearing term, both the

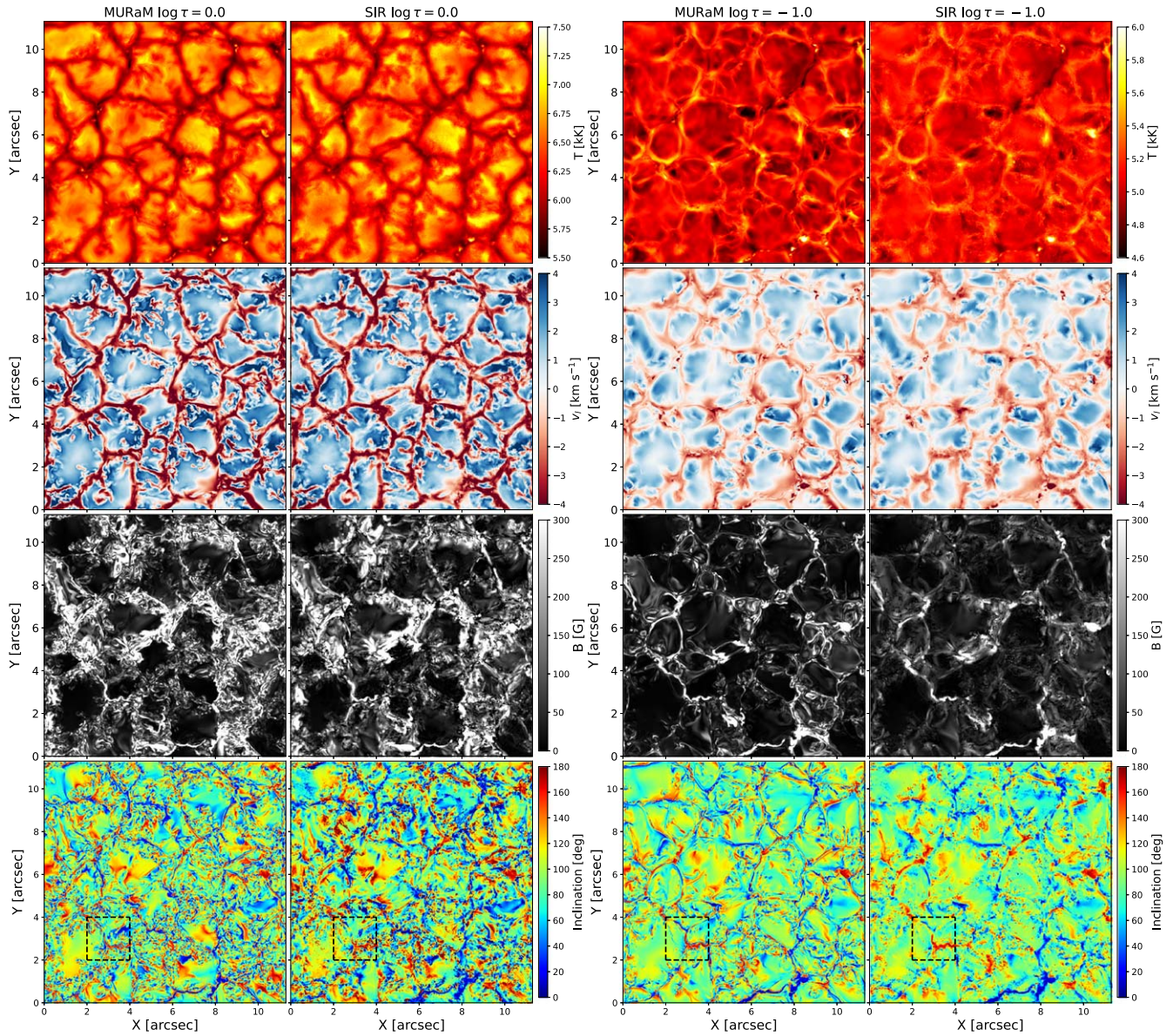

Figure 8. Comparison between the ground-truth atmosphere (first and third columns) and that inferred with SIR (second and fourth columns). The left two columns show the comparison at $\log\tau = 0$ and the right two columns show the comparison at $\log\tau = -1$. From top to bottom, we show the temperature, LOS velocity, magnetic field strength, and inclination. An example of a mixed-polarity region is marked with black dashed boxes.

unsigned and signed versions show qualitative agreement with the ground truth: strong values are concentrated along the granular lanes. The absolute values of all three are underestimated overall, as evidenced by the histogram. The signed shearing term, in addition, tends to be more negative than the ground truth. The histograms show an obvious skew toward the negative side. As expected, the estimated Poynting fluxes are always smaller than the ground truth. For the shearing term, the negative fluxes are more consistent with ground truth than the positive fluxes, resulting in an overall underestimation. The inferred unsigned Poynting flux is $2.0 \times 10^8\,\mathrm{erg\,cm^{-2}\,s^{-1}}$, which is 53.9% of the ground truth. The emergence term of Poynting flux is 33.6% of the ground truth, while the shearing term of Poynting flux is only 17.3%. The unsigned shearing term of Poynting flux is $9.5 \times 10^7\,\mathrm{erg\,cm^{-2}\,s^{-1}}$, which is 44.6% of the ground truth. The net Poynting flux is $-1.1 \times 10^7\,\mathrm{erg\,cm^{-2}\,s^{-1}}$, which has a wrong sign and is far from the ground-truth value of $3.7 \times 10^6\,\mathrm{erg\,cm^{-2}\,s^{-1}}$.

Most conclusions for $\log\tau = 0$ hold true for $\log\tau = -1$, while the underestimation becomes more severe. For the shearing term, a large fraction of the strong-flux pixels are not recovered. The predominant positive shearing term is also missing. The distribution of S_z^{sh} is much narrower around 0 compared to the ground truth, with too few positive pixels and a small excess of negative pixels.

5. Discussion

In Section 3, we show that DAVE4VMwDV has reasonable performance when applied to the high-resolution simulation data directly. However, the Poynting flux is significantly underestimated. As expected, the case is more severe for the emulated observation case, and we find the main culprit is the

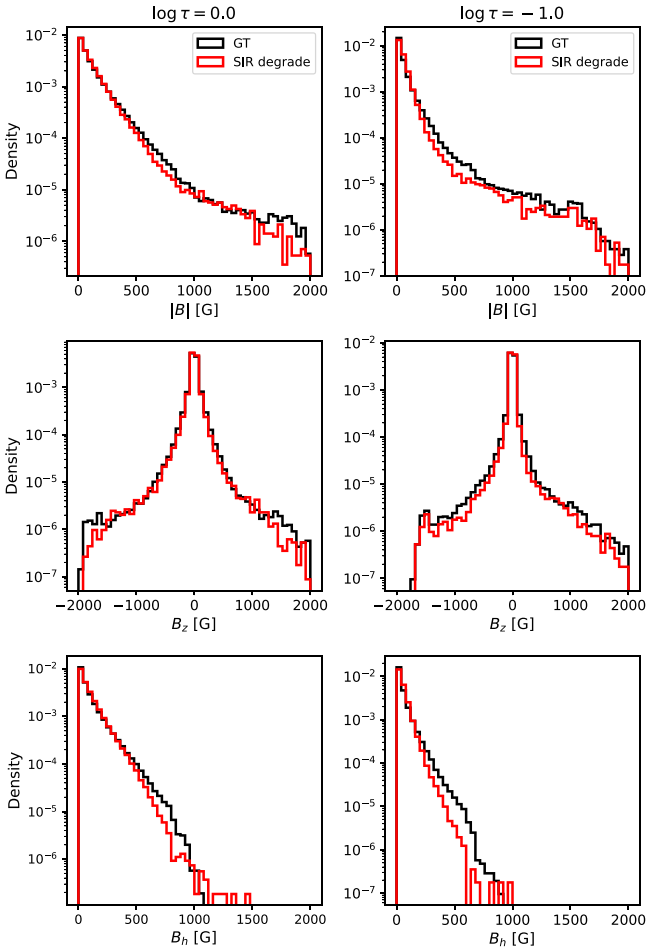

Figure 9. Comparison of the distributions of the ground truth (black) and inverted magnetic field (red). Left: histograms of quantities at $\log\tau = 0$. Right: histograms of quantities at $\log\tau = -1$. The figure shows the distribution of the magnetic field strength $|B|$, vertical magnetic field B_z, and horizontal magnetic field B_h. The inversion results have lower resolution and thus fewer pixels, and the histograms are all normalized for comparison.

shearing term. We investigate below the quality of the inferred magnetic and velocity fields in an attempt to address the "missing Poynting flux."

5.1. Quality of Inferred Velocity

DAVE4VMwDV infers the velocity field from magnetograms by minimizing the residual of the ideal induction equation. In our work, we apply DAVE4VMwDV on magnetograms, i.e., magnetic field maps, at the same optical depth where the spatial derivatives are poorly defined. Thus, the ideal induction equation does not strictly hold, particularly at small spatial scales, where the τ surface is corrugated. Below, we assess how well the ideal assumption is satisfied and how it affects the inferred velocity at spatial scales.

To this end, we evaluate the power spectral density (PSD) of the inferred variables. For a square FOV in Cartesian coordinates (i.e., $n_x = n_y = N$ and $\Delta x = \Delta y$), the PSD(k) as a function of the wavenumber is computed as

$$\mathrm{PSD}(k) = N\Delta x \sum_{k'\in[k,k+dk]} |\tilde{f}(k')|^2, \tag{12}$$

where $\tilde{f}$ is the 2D Fourier transform for an arbitrary spatial function f, and $k = \sqrt{k_x^2 + k_y^2}$ is the square root of the wavenumber in the x-direction (k_x) and y-direction (k_y).

The PSDs for the two terms of the induction equation, $\partial B_z/\partial t$ and $(\nabla \times \boldsymbol{E})_z$, and the three components of velocity at $\log\tau = 0$ and $\log\tau = -1$ are shown in Figure 14. The values are normalized by their maxima. As seen in the top row, the two terms of the induction equation from the MHD simulation at the same optical depth are not entirely consistent, especially in the scale $d < 120$ km (top row, black and red curves). This is because the maps ($\boldsymbol{B}$ and $\boldsymbol{v}$) we use are at the same τ surface, which may correspond to different z at different times. The spatial derivatives made in a constant-τ surface may also contribute to the mismatch. This significantly affects the quality of inferred velocity based on the sampled ground-truth magnetograms: a large discrepancy of PSD in the small-scale regime ($d < 150$ km). The agreement is somewhat worse for $\log\tau = -1$ compared to $\log\tau = 0$.

For the performance of DAVE4VMwDV on emulated observations, we only plot the PSD for $\partial B_z/\partial t$ in Figure 14. At $\log\tau = 0$, the PSD deviates significantly from the ground truth even at large spatial scales (top row, blue curves). Quite interestingly, the mismatch does not appear to affect much the accuracy of the inferred velocity field on a large scale. The PSDs of all three components of the DAVE4VMwDV velocity closely follow the ground truth for $d < 300$ km. Again, the results are similar but better for $\log\tau = -1$. In particular, the PSD of $\partial B_z/\partial t$ agrees well with the reference at scales $d > 250$ km.

To quantify the Poynting flux response with respect to the scale of the velocity, we decompose the ground-truth velocity fields according to their spatial scales:

$$\begin{aligned} v_z &= v_z^h + v_z^l, \\ \boldsymbol{v}_h &= \boldsymbol{v}_h^h + \boldsymbol{v}_h^l, \end{aligned} \tag{13}$$

where the superscripts h and l represent the high-frequency part and the low-frequency part of the quantity. The Poynting fluxes can then be decomposed in a similar fashion as they are linear with respect to the velocity:

$$\begin{aligned} S_z &= S_z^h + S_z^l, \\ S_z^l &= \frac{1}{4\pi}\int_S \boldsymbol{B}_h^2 v_z^l dS - \frac{1}{4\pi}\int_S (\boldsymbol{B}_h \cdot \boldsymbol{v}_h^l) B_z dS, \\ S_z^h &= \frac{1}{4\pi}\int_S \boldsymbol{B}_h^2 v_z^h dS - \frac{1}{4\pi}\int_S (\boldsymbol{B}_h \cdot \boldsymbol{v}_h^h) B_z dS. \end{aligned} \tag{14}$$

The relation between the two terms of S_z^l is shown in Figure 15. The upper panel shows the variation of the absolute values of $\langle S_z^{\mathrm{em}}\rangle$ and $\langle S_z^{\mathrm{sh}}\rangle$ with respect to the scale of the velocities d. The shearing term of the Poynting flux has a steep slope: the small-scale velocity plays an important role. At $\log\tau = 0.0$, the two terms almost cancel each other out, and the net Poynting flux tends to be negative for large-scale velocity. The result at $\log\tau = -1.0$ differs from that at $\log\tau = 0.0$ mainly for small scales $d < 400$ km. The magnitude of the shearing term is about twice that of the emergence term, which results in a clear net positive Poynting flux.

The bottom panels of Figure 15 show the ratio of S_z^l to the ground-truth S_z with respect to the scale of the velocity d. To recover 80% of the shearing term of the Poynting flux, the horizontal velocity $\boldsymbol{v}_h$ should have scales $d > 156$ km and

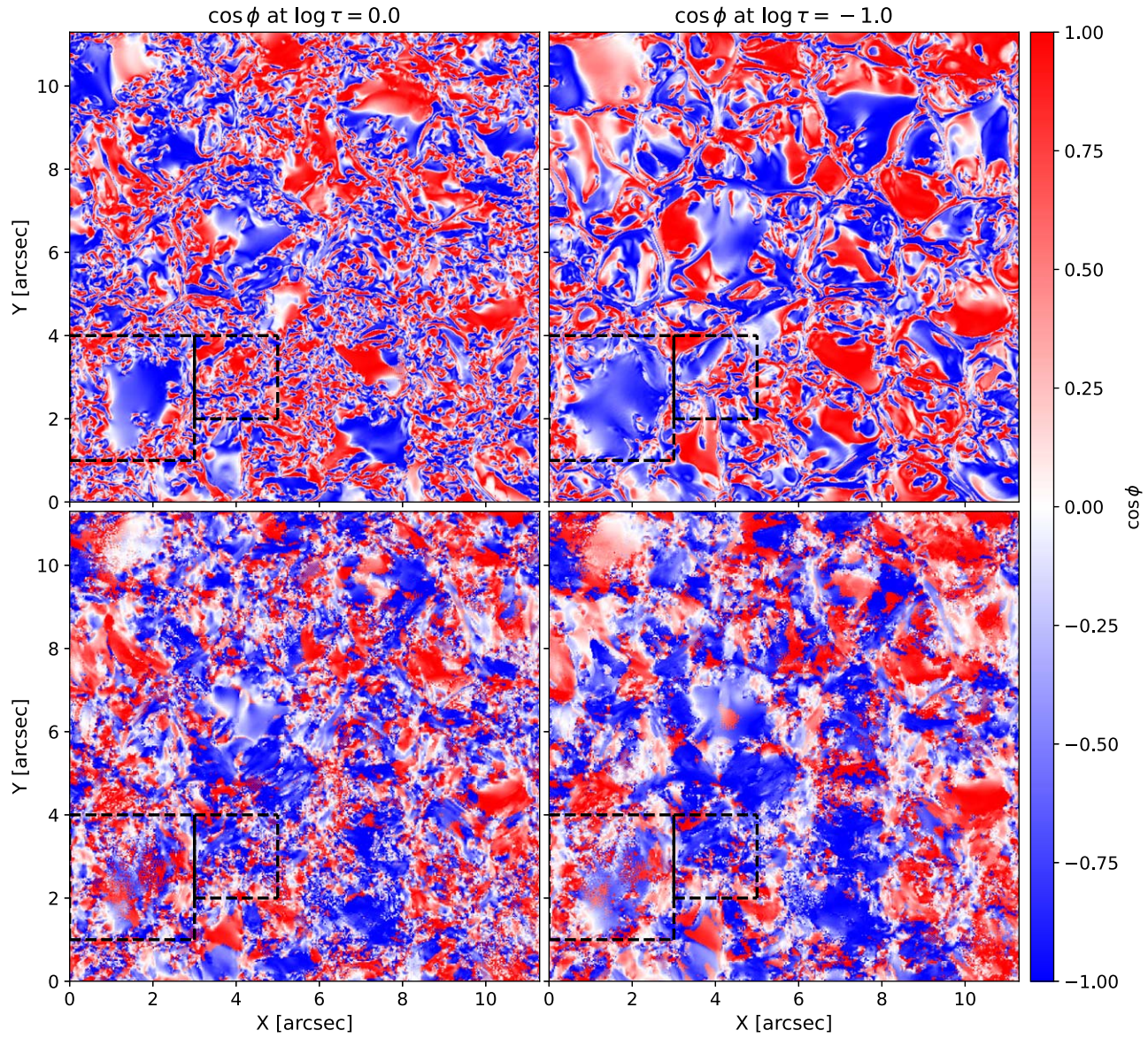

Figure 10. Comparison of the cosine of the azimuth between ground truth (upper row) and the one inferred with SIR after disambiguation (bottom row). From left to right we show the comparison at $\log\tau = 0$ and $\log\tau = -1$. Two dashed black boxes mark regions discussed in Section 4.1.

$d > 145$ km at $\log\tau = 0$ and -1.0, while a vertical velocity v_z with $d > 834$ km and $d > 625$ km can recover 80% of the emergence term of the Poynting flux at $\log\tau = 0$ and -1.0. At a scale of $d > 150$ km, the shear term is 80.8% and 79.1% of the ground-truth value at $\log\tau = 0.0$ and -1.0, respectively, and the emergence term is 100% and 100%, respectively, which are close to the calculations of DAVE4VMwDV in Section 3.

We point out that the simulation output itself, which we use as the ground truth, may not strictly adhere to the ideal induction equation due to numerical diffusion. We compare $\partial B_z/\partial t$ and $(\boldsymbol{\nabla} \times (\boldsymbol{v} \times \boldsymbol{B}))_z$ on constant-z slices. While the overall agreement is better than that for the constant-τ slices shown in the first row of Figure 14, the scatter becomes significantly greater below about the 100 km scale. This suggests that the numerical effect of the input likely also contributes to the discrepancy. For real-Sun observations, such nonideal effects may come from small-scale, turbulent magnetic fields and velocities, which manifest as a second-order term in the induction equation that cannot be averaged to zero. It remains to be seen whether high-resolution observations from DKIST can help alleviate the issue.

One interesting takeaway from Figure 15 is that the induction equation (i.e., $\partial B_z/\partial t$ and $(\nabla \times \boldsymbol{E})_z$) is dominated by the spatial scale of a few hundred kilometers in this quiet-Sun simulation. As the geometric height of the input magnetograms (constant τ) varies, one does not expect the induction equation to be well satisfied numerically beyond such size. Since DAVE4VMwDV solves for the induction equation "locally" by minimizing the residual within a small window, it might be more suited for quiet-Sun calculations compared to other, more "global" algorithms.

5.2. The Limitation in Stokes Inversion

The second factor that can affect the estimate of Poynting flux is the magnetograms inverted with SIR. From Equation (8), the

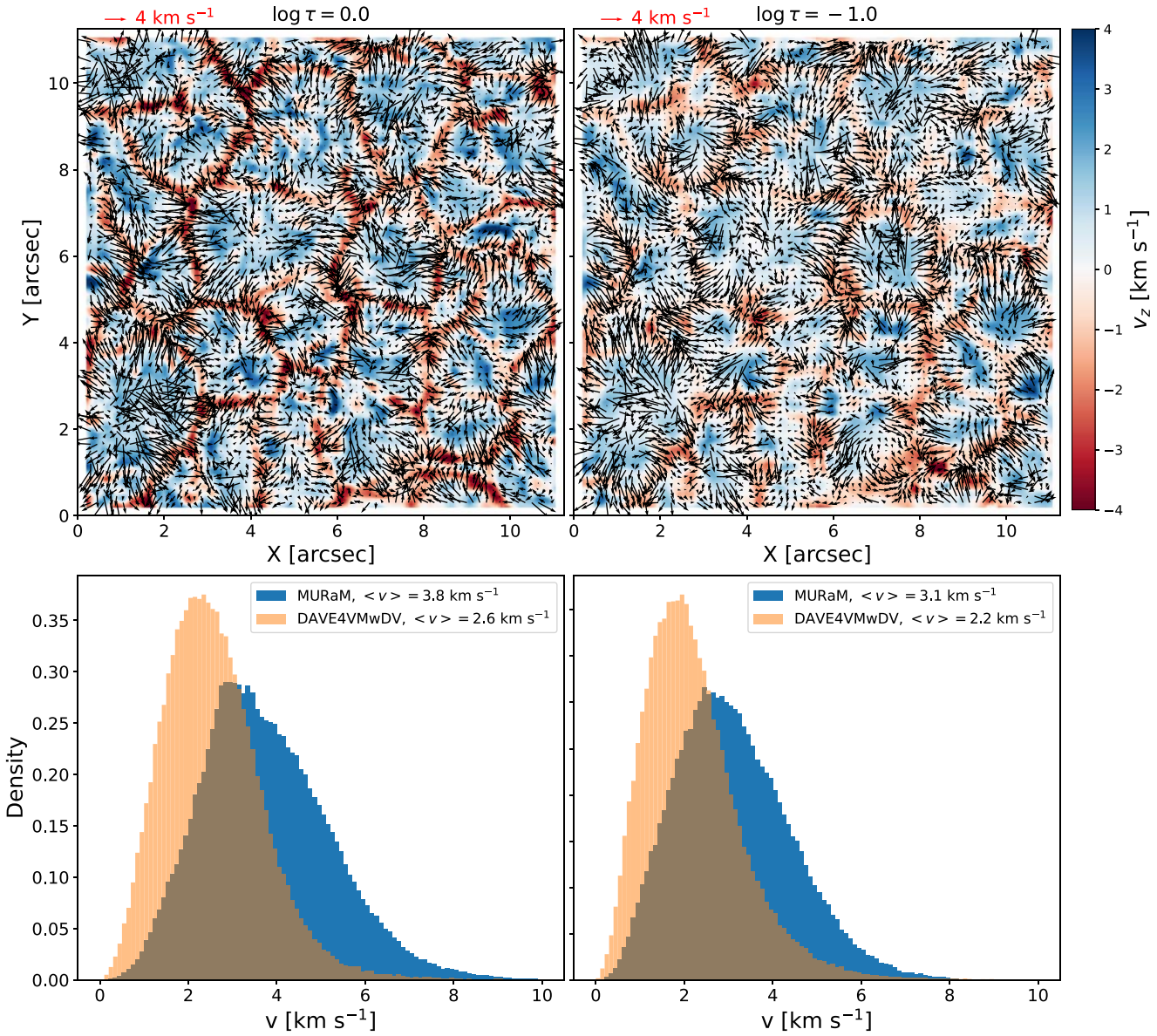

Figure 11. Velocities inferred from inverted magnetograms at $\log\tau = 0.0$ (left) and $\log\tau = -1.0$ (right). Top: the inferred velocity field. The horizontal arrows indicate the direction and amplitude of the horizontal velocity. The vertical velocities are plotted as the background. Bottom: histograms of the magnitude of the ground-truth velocity (blue) and inferred velocity (orange).

emergence term of the Poynting flux $|S_z^{\rm em}| \propto B_h^2$ and the shearing term $|S_z^{\rm sh}| \propto |B_h B_z|$. As demonstrated in Figure 9, the inaccuracies of the inferred magnetic field can affect the downstream velocity and the Poynting estimates.

One likely factor is the fact that we reduce the spatial resolution of the Stokes profiles before inversion, which is known to affect the retrieved magnetic field distribution (e.g., I. Milic et al. 2024). The other factor is the inversion algorithm itself, for example, the node-based representation of the variables. As stated in Section 2, to reduce the number of free parameters, SIR perturbs the initial atmosphere only in the location of nodes and approximates the remaining atmosphere with cubic spline interpolation. In our work, we apply five nodes in the atmosphere range in $\log\tau = [-4.2, 1.0]$. The locations of nodes in the range $\log\tau = [-2.0, 0]$ (the typical range of formation height for the Fe I 630 nm lines) are $\log\tau = -0.3$ and -1.6. As the structure of the atmosphere is unknown a priori, the ground-truth stratification may not be faithfully represented by a five-node function.

To investigate the effect of these factors, we conduct two more inversion experiments. For the first experiment, we keep the same configuration in Table 1 for SIR, but use synthetic Stokes without degradation. This experiment aims to assess the effects of the PSF and rebinning. For the second experiment, we use the SIR configuration listed in Table 3 on the same input without degradation. We increase the number of nodes for the magnetic field strength, inclination, and azimuth to 14, 14, and 5. The locations of nodes for magnetic field strength and inclination in the range $\log\tau = [-2, 0]$ are $[-0.2, -0.6, -1.0, -1.4, -1.8]$.

The histograms of the total, vertical, and horizontal magnetic fields from the two experiments, along with the reference values at optical depths $\log\tau = 0.0$ and -1.0, are shown in Figure 16. For the first experiment (blue lines), the distributions

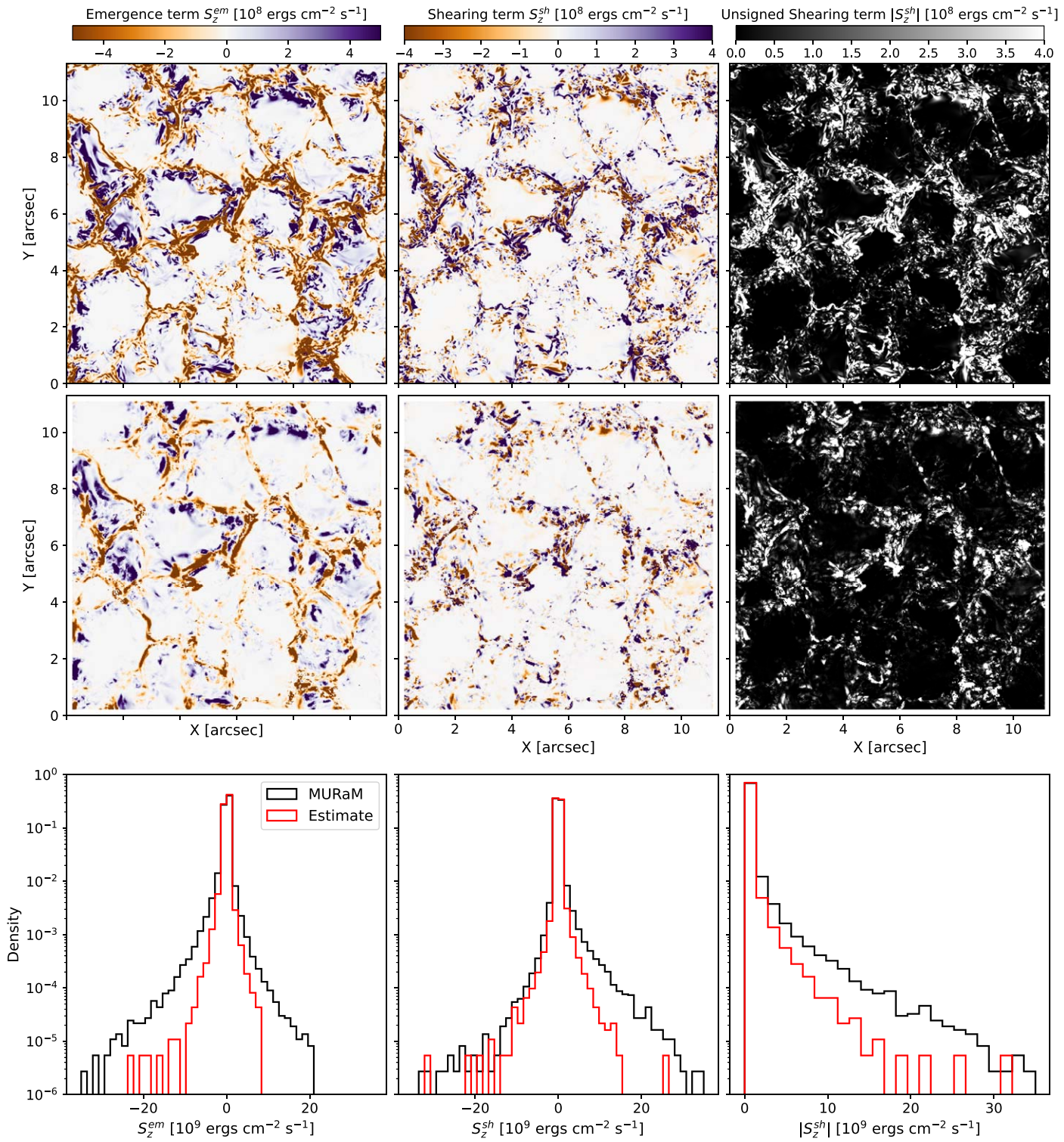

Figure 12. Comparison between MURaM and estimated Poynting flux at $\log\tau = 0$. Top: ground-truth value of the Poynting flux. Middle: estimated Poynting flux with inferred magnetic and velocity fields. Bottom: histograms of Poynting flux from ground truth (black) and estimate (red). From left to right are the emergence term, shearing term, and unsigned shearing term of the Poynting flux.

of the inverted magnetic field still deviate from the reference value. But at $\log\tau = 0$, the relative number of pixels with $|B|$ > 800 G and $B_h > 750$ G is now greater than the reference, which is the opposite of the result of inversion on degraded data. At $\log\tau = -1$, there are also deviations for $|B|$ in the range of [250, 750] G and $B_h > 250$ G. The distribution of B_z is smaller than the reference. The result of this experiment suggests that the degradation alone cannot fully account for the mismatch in the magnetic field distribution. The inversion process itself must also contribute.

For the inversion experiment with additional nodes, the distributions of the inverted magnetic fields are greater than the

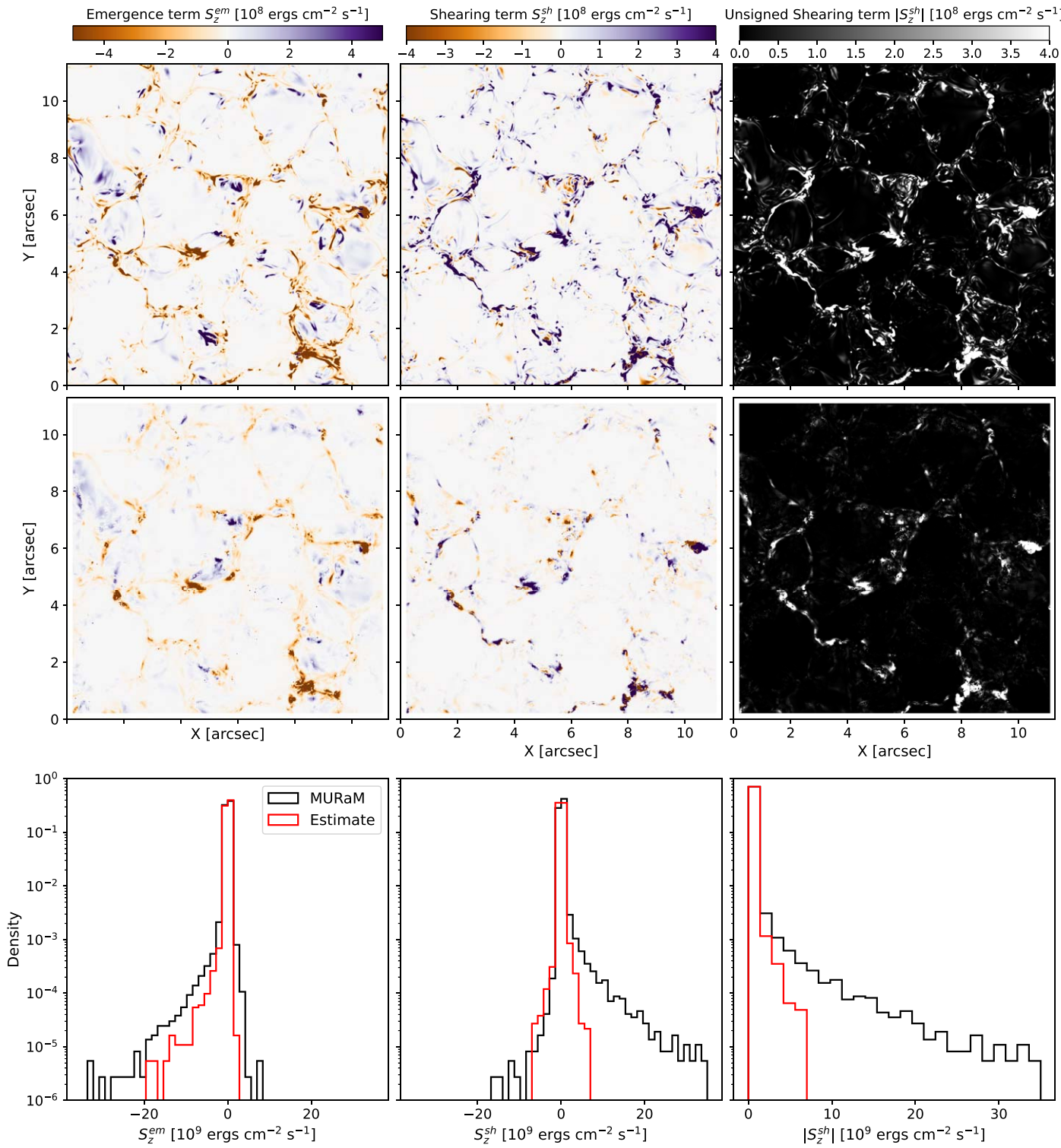

Figure 13. Same as Figure 12, but for $\log\tau = -1$.

reference at $\log\tau = 0.0$. At $\log\tau = -1.0$, the distributions of B and B_z are closer to the reference distributions. But the distribution of B_h is greater than the reference at $B_h > 700$ G. This suggests that fitting with more nodes may recover a more accurate distribution (A. Pastor Yabar et al. 2019). In practice, the optimal number of nodes cannot be determined a priori. Overfitting may be a concern.

The PSDs of magnetic field strength for the two experiments, the inversion from the emulated observation, and the reference are shown in Figure 17. Compared to the reference, the overall quality of the inferred magnetic field strength is reasonable on larger spatial scales ($d \gtrsim 200$ km), and disagreement becomes obvious on smaller scales. Additionally, the result of the emulated observation displays an excess in PSD at the largest

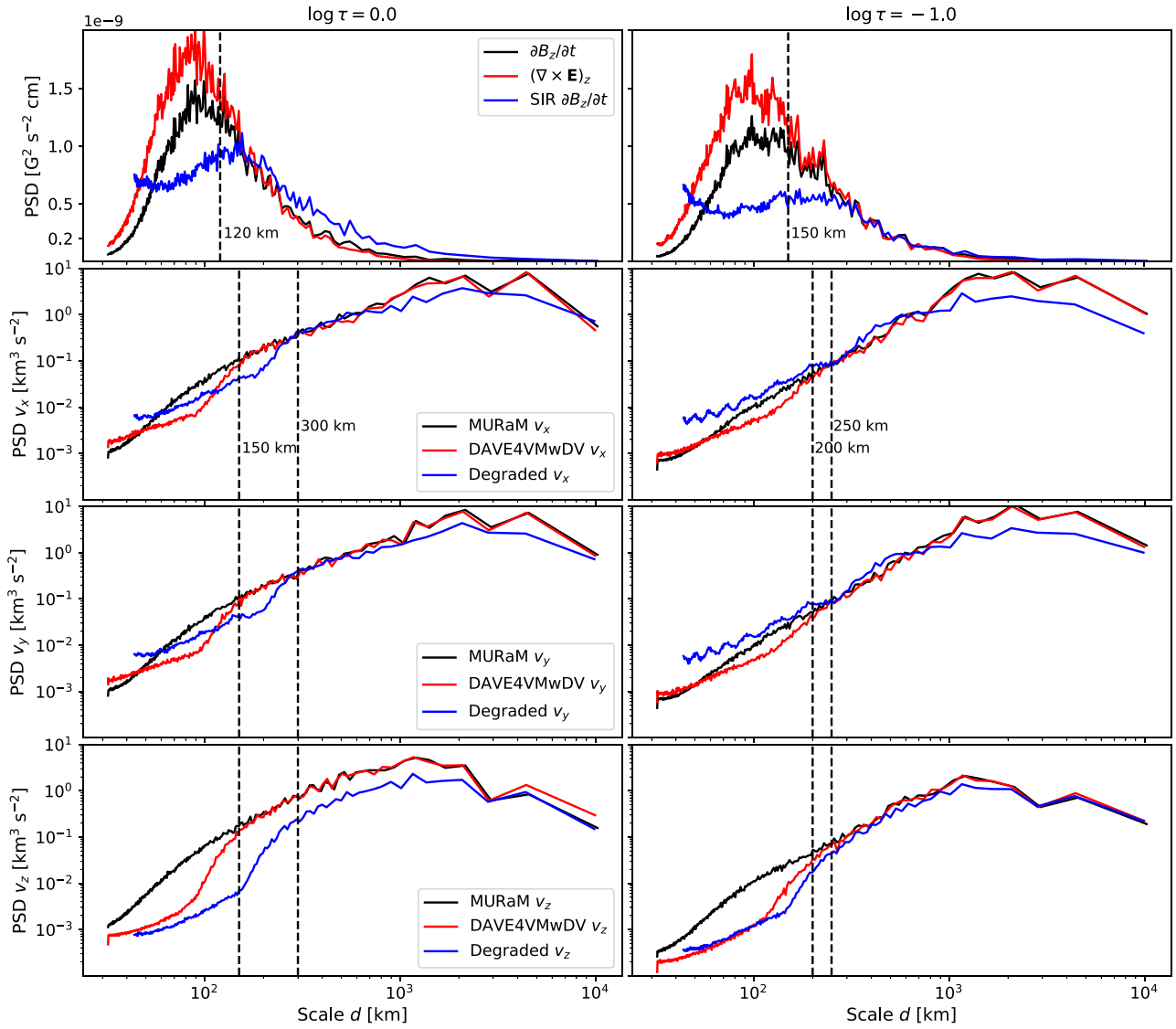

Figure 14. PSD for selected inferred variables as a function of scale d at optical depth $\log\tau = 0$ (left) and $\log\tau = -1$ (right). From top to bottom: PSD of two terms in the induction equation, v_x, v_y, and v_z. In the top panel, the black line represents the ground-truth time derivative of the vertical magnetic field, the red line represents the vertical component of the curl of the electric field $\boldsymbol{E} = -\boldsymbol{v} \times \boldsymbol{B}$, and the blue line represents the time derivative of the inferred vertical magnetic field. In the second to the last row, the black line represents the ground-truth velocity, the red line represents the velocity inferred directly from the MURaM magnetograms (Section 3), and the blue line represents the result from the velocity inferred from the emulated observation (Section 4). The PSDs of variables inferred from degraded synthetic data do not reach the smallest scales in the figure due to their lower resolution. The vertical dashed lines highlight the spatial scale, below which large discrepancies exist between the ground truth and the inference.

scale ($d \gtrsim 4 \times 10^3$ km), about half of the domain size. The reason for such an excess is unclear.

To investigate the effect of inversion on estimating Poynting flux, we calculate the Poynting flux with inferred magnetograms and ground-truth velocities. Since there is still a problem in disambiguation, we only consider the emergence term ($S_z^{\rm em}$) and the absolute value of the shearing term ($|S_z^{\rm sh}|$). The comparison between the two experiments and ground truth is shown in the last two rows of Figure 16. At $\log\tau = 0.0$, as a result of greater relative numbers of large B_z and B_h in both experiments, the probability density distributions of $S_z^{\rm em}$ and $|S_z^{\rm sh}|$ of the two experiments are greater than the reference, especially in the negative part of $S_z^{\rm em}$. The results at $\log\tau = -1.0$ are different since, given the deviation in the distribution of the magnetic field, $S_z^{\rm em}$ and $|S_z^{\rm sh}|$ both have smaller density than the reference for the first experiment. For the second experiment, the probability density distributions are close to the reference for both $S_z^{\rm em}$ and $|S_z^{\rm sh}|$. The average emergence terms of the Poynting fluxes are 106.1% and 147.0% of the reference at $\log\tau = 0.0$, and 92.8% and 99.3% of the reference at $\log\tau = -1.0$ for the two experiments, respectively. The average unsigned shearing terms of the Poynting fluxes are 116.9% and 127.1% of the reference at $\log\tau = 0.0$, and 78.3% and 105.9% of the reference at $\log\tau = -1.0$ for the two experiments, respectively. The results suggest that the missing magnetic flux and the overestimated magnetic flux from the inversion can result in a missing Poynting flux and an overestimated Poynting flux.

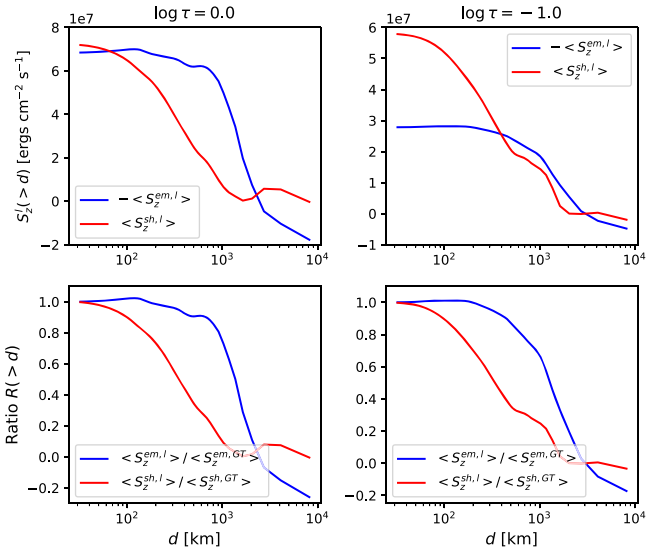

Figure 15. The response of the emergence term $S_z^{\rm em}$ and shearing term $S_z^{\rm sh}$ of Poynting flux to the scale of velocity at $\log\tau = 0$ (left) and $\log\tau = -1$ (right). Top: the response of the absolute values to scale. Bottom: the response of the ratio of the value to ground truth. The red and blue lines represent the shearing term and emergence term, respectively.

Table 3
Summary of SIR Algorithm Configurations for Experiment Two

Parameters	Nodes			
	Cycle 1	Cycle 2	Cycle 3	Cycle 4
Temperature	2	3	5	5
Microturbulence	1	1	1	1
LOS velocity	1	2	3	5
Magnetic field strength	1	2	3	14
Inclination	1	2	3	14
Azimuth	1	2	2	5

5.3. Energy Transport in Quiet-Sun Photosphere

Studying the energy transport in the quiet-Sun photosphere is difficult. Besides the difficulties in observation and inversion of Stokes profiles, another concern is that due to the weaker magnetic fields, the plasma $\beta = 8\pi p/B^2$ in the quiet-Sun photosphere varies more rapidly in space compared to that in active regions. The dynamic characteristics and the importance of the Poynting flux in energy transfer may change drastically with height. To demonstrate this, we plot the median plasma β as a function of the logarithm median optical depth $\log\langle\tau\rangle$ at each height in the top panel of Figure 18. The median plasma β in the $\log\langle\tau\rangle \in [0, -2]$ layer has a value of about 10^4, suggesting that the plasma kinematics dominate the magnetic fields. The behavior is quite different for regions with stronger magnetic fields (e.g., granular lanes). The plasma β, where the magnetic field strength is greater than three times the standard deviation at each height ($B > 3\sigma_B$), has a value below 10.

In the middle panel of Figure 18, we show the net Poynting flux density variation with height. The net Poynting flux increases with height in the range $\log\langle\tau\rangle = [1, -0.5]$ and the

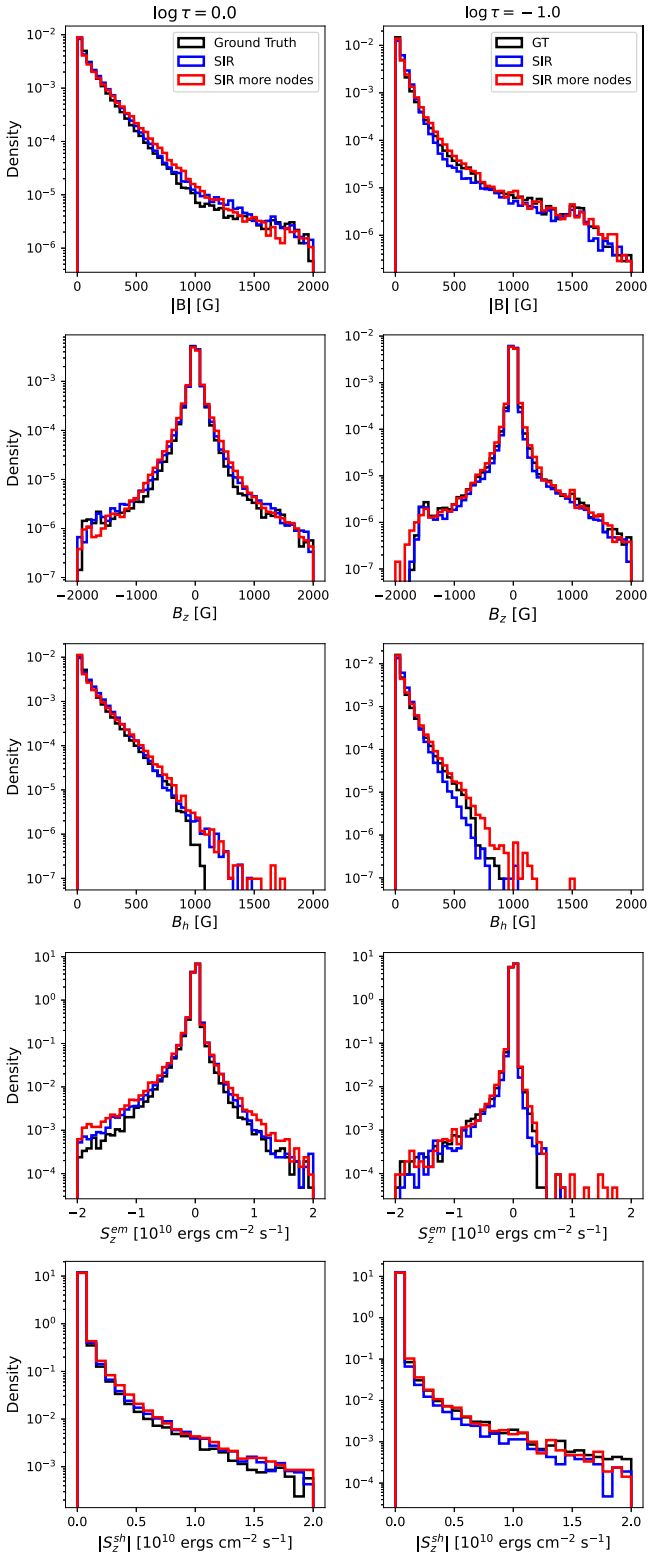

Figure 16. Comparison of the distributions of quantities from the reference magnetic field (black), the inverted magnetic field with the configuration in Table 1 (blue), and that with the configuration in Table 3 (red) at $\log\tau = 0.0$ (left) and $\log\tau = -1.0$ (right). From top to bottom, we show the distribution of the magnetic field strength $|B|$, the vertical magnetic field B_z, the horizontal magnetic field B_h, the emergence term of the Poynting flux $S_z^{\rm em}$, and the unsigned shearing term of the Poynting flux $|S_z^{\rm sh}|$.

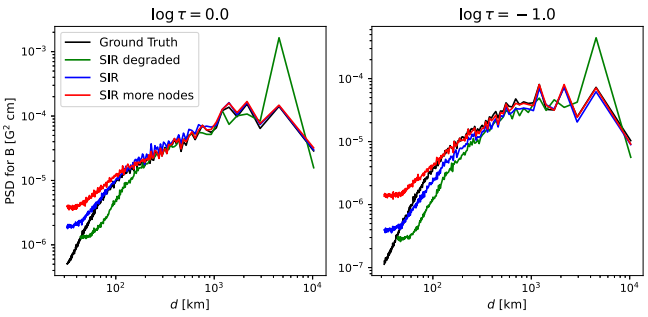

Figure 17. Comparison of the PSD of magnetic field strength from the reference magnetic field (black), inversion from the emulated observation (green), the inverted magnetic field with the configuration in Table 1 (blue), and that with the configuration in Table 3 (red) at $\log\tau = 0.0$ (left) and $\log\tau = -1.0$ (right).

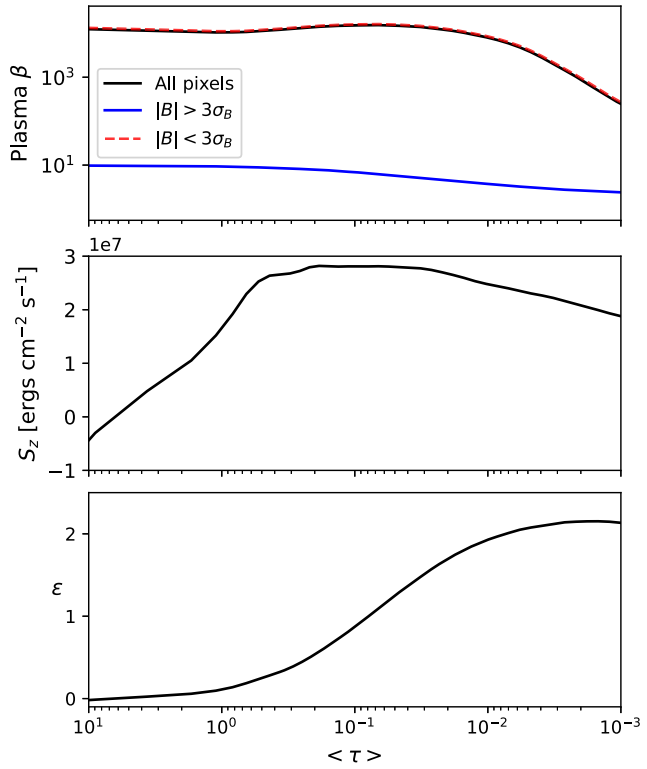

Figure 18. Top: plasma β in the region of interest with respect to height. The black, blue, and red lines represent the plasma β averaged among all the pixels, pixels with $B > 3\sigma_B$, and pixels with $B < 3\sigma_B$ in the region of interest, respectively. Middle: variation of net Poynting flux density with height. Bottom: fraction of energy transported by the Poynting flux relative to energy converted by the Lorentz force.

value changes from $-4.0 \times 10^6\,\mathrm{erg\,cm^{-2}\,s^{-1}}$ to $2.6 \times 10^7\,\mathrm{erg\,cm^{-2}\,s^{-1}}$. The net Poynting flux gradually decreases in the atmosphere higher than $\log\langle\tau\rangle = -0.5$.

In the bottom panel of Figure 18, we calculate the contribution to energy change by Poynting flux. We calculate the ratio ϵ between the Poynting flux at a certain height z and the total magnetic energy change above height z, as a function of $\log\langle\tau\rangle$ for each z:

$$\epsilon = \frac{S_z(z)}{dE_m/dt}. \tag{15}$$

Here, the calculation is done on the entire box so the Poynting flux through the side boundary can be ignored. We also ignore the Poynting flux leaving the top boundary because its value is small (M. Rempel 2014). At the height with $\log\langle\tau\rangle = 0.0$, Poynting flux only contributes 11.2% of the change of magnetic energy. This changes drastically at $\log\langle\tau\rangle = -1.0$: Poynting flux contributes 87.3% of the magnetic energy change, suggesting that it is the main source of magnetic energy change in the typically observed photospheric layer even under the non-force-free condition.

5.4. Implications on Observations

In a recent work, D. Tilipman et al. (2023) studied the Poynting flux in the quiet-Sun photosphere with real observations from the balloon-borne SUNRISE/IMaX data. They used two different codes based on deep learning and correlation tracking to infer the velocity and calculate the Poynting flux at $\log\tau \approx 0$. They found that there is not enough Poynting flux except in strong-field regions. Similar to our study on emulated observations, they found that the shearing term of Poynting flux is underestimated. The emergence term dominates both the total and unsigned Poynting flux, though the mean value was positive in their observation while it is negative in our study. The difference in sign may be attributed to the strong magnetic field in the upflow region of their region of interest, while the emergence term of Poynting flux is concentrated on the intergranular lane. The fraction of emergence term on the unsigned Poynting flux is 99% in their observation; the fraction is 92% in our study. The small difference may be attributed to the use of different flow tracking methods. The ability of different flow tracking methods to estimate Poynting flux requires more investigation.

The work of D. Tilipman et al. (2023) used a Milne–Eddington inversion code, which assumes a constant magnetic field with height. Such a simplifying assumption is appropriate due to the limited spectral resolution of SUNRISE/IMaX. However, according to the MURaM simulation (Figure 18), the Poynting flux in the quiet Sun has a large variation with height. A single Poynting flux estimate at $\log\tau \approx 0$ is not necessarily representative.

6. Conclusion

In this work, we assess the diagnostic capability of the DL-NIRSP instrument on DKIST for the energy transport processes in the quiet-Sun photosphere with the realistic numerical MHD simulation code MURaM. We first validate the widely used and recently modified flow tracking algorithm DAVE4VMwDV high-resolution data. We then synthesize and degrade high spatial and temporal resolution Stokes profiles of the Fe I 630 nm lines to emulate the observation made by DKIST/DL-NIRSP and infer the vector magnetic field maps. Finally, we examine the estimated Poynting flux from the emulated observation.

Our main findings are as follows:

1. DAVE4VMwDV works reasonably well on inferring the photospheric velocity on high-resolution data, especially the large-scale ($d > 150$ km) velocity. At smaller scales, the corrugated τ surface results in the induction equation being poorly satisfied via numerical differentiation; the accuracy of the velocity inference thus suffers. For the emulated observation, the ill-satisfied induction equation does not impact the large-scale velocity much.

2. The temporal resolution of input magnetograms can affect the performance of DAVE4VMwDV. To get a reasonable velocity estimate, we suggest the input magnetograms and Dopplergrams have $\Delta x/\Delta t > \langle v \rangle$.
3. The Poynting flux calculated with the inferred velocity similarly matches the ground truth better at larger spatial scales. The average value is underestimated in both simulation and emulated observation. In the emulated observation, the estimated unsigned Poynting flux is about 72.5% and 61.3% of the reference ground truth at $\log\tau = 0.0$ and $\log\tau = -1.0$. The net Poynting flux is $-1.3 \times 10^7\,\mathrm{erg\,cm^{-2}\,s^{-1}}$ and $-8.5 \times 10^6\,\mathrm{erg\,cm^{-2}\,s^{-1}}$, compared to ground truth: $3.7 \times 10^6\,\mathrm{erg\,cm^{-2}\,s^{-1}}$ and $3.0 \times 10^7\,\mathrm{erg\,cm^{-2}\,s^{-1}}$.
4. The main difference comes from the underestimated shearing term. The estimated net emerging Poynting flux can reproduce 99.6% and 88.8% of the ground-truth net emerging Poynting flux, while the net shearing Poynting flux is only 72.0% and 55.5% of the ground truth.
5. The net shearing term of the Poynting flux is more difficult to estimate than the net emergence term of the Poynting flux. To recover 80% of the shearing term of the Poynting flux, the inferred horizontal velocity field should have a spatial scale $d > 156$ km and $d > 145$ km at $\log\tau = 0$ and -1. To recover 80% of the emergence term of the Poynting flux, the inferred vertical velocity field should have a spatial scale $d > 834$ km and $d > 625$ km.

Estimating energy transport on the photosphere of the quiet Sun is difficult. The inferences of the magnetic field and the velocity field must both be improved for a better estimate of the Poynting flux. For magnetic field inversion, new advances have been made by including the more realistic magnetohydrostatic equilibrium assumption (compared to the commonly used hydrostatic equilibrium; A. Pastor Yabar et al. 2019), or using deep learning algorithms (A. Asensio Ramos & C. J. Díaz Baso 2019; K. E. Yang et al. 2024). These methods can resolve azimuthal ambiguity, and provide an absolute spatial scale along the LOS, which produces magnetic field maps on a constant geometric height. The latter makes the application of velocity tracking a self-consistent approach, and can also reduce the effect of the p-mode that would imprint on the τ surface (M. Rempel 2024, private communication). To demonstrate the possible improvement, we apply DAVE4VMwDV on the MURaM simulation at two constant geometric heights with $\langle \log\tau \rangle = 0.02$ and $\langle \log\tau \rangle = -1.02$. At these two heights, 82.9% and 74.5% of the shearing term can be recovered, which shows an about 10% and 20% increase as compared to the results for the constant-τ surfaces.

For velocity inference, new algorithms based on deep learning, such as DeepVel (A. Asensio Ramos et al. 2017), have shown much potential. High spectral and spatial resolution observations from DKIST and multi-spectral-line Stokes inversions will also allow for estimates of the velocity field or electric field at multiple heights simultaneously. This is expected to improve the study on the energy transport in the solar atmosphere above the quiet Sun.

In addition, the signal-to-noise level is another important factor in estimating the Poynting flux. C. Quintero Noda et al. (2023) studied the effect of noise on Stokes inversion. Their study suggested that the inversion of data with a noise level on the order of or lower than 5×10^{-4} of the continuum intensity can provide more reliable information for the vector magnetic fields. The details of how noise affects the Poynting flux estimate will be investigated in the future.

Acknowledgments

We thank Carlos Quintero Noda and Matthias Rempel for their valuable input. Support for this work is provided by the National Science Foundation through the DKIST Ambassadors program, administered by the National Solar Observatory and the Association of Universities for Research in Astronomy, Inc. X.S. is additionally supported by NSF Awards #2008344 and #1848250.

Appendix A
Optimization of DAVE4VMwDV

Besides the magnetogram and Dopplergram input, DAVE4VMwDV has three free parameters: the window size w for optimization, the maximum degree of Legendre polynomials d for velocity expansion inside the window, and the relative weighting λ for term L_2 defined in Equation (6). In this work, we optimize these parameters using the methods described in X. Sun et al. (2023). The initial parameters are $w = 15$, $d = 3$, and $d_r = 5$.

A.1. DAVE4VMwDV on MHD Simulation

We first use the "L-curve," which displays the trade-off between the two terms as λ varies (e.g., P. C. Hansen & D. P. O'Leary 1993), to determine λ. Figure 19 shows the curves of normalized (L_1, L_2) with varied λ at $\log\tau = 0$ and $\log\tau = -1$ for the application to the MHD data. The point $\lambda = 0$ represents the case of DAVE4VM, where the Doppler constraint is not considered. At $\log\tau = 0.0$, both L_1 and L_2 decrease as λ increases, while at $\log\tau = -1.0$, the curve resembles an

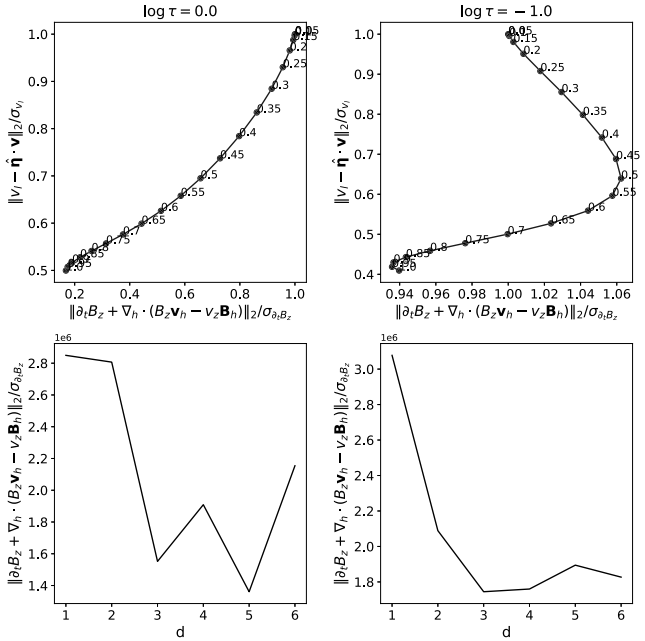

Figure 19. Parameter selection for DAVE4VMwDV for MHD data at $\log\tau = 0$ (left) and $\log\tau = -1$ (right). Top: L-curve displaying the trade-off between the two loss function terms L_1 and L_2 in DAVE4VMwDV. The values next to the black dots represent the weighting λ of each test. Bottom: the variation of the loss function term L_1 with respect to the degree of Legendre expansion in the horizontal direction d.

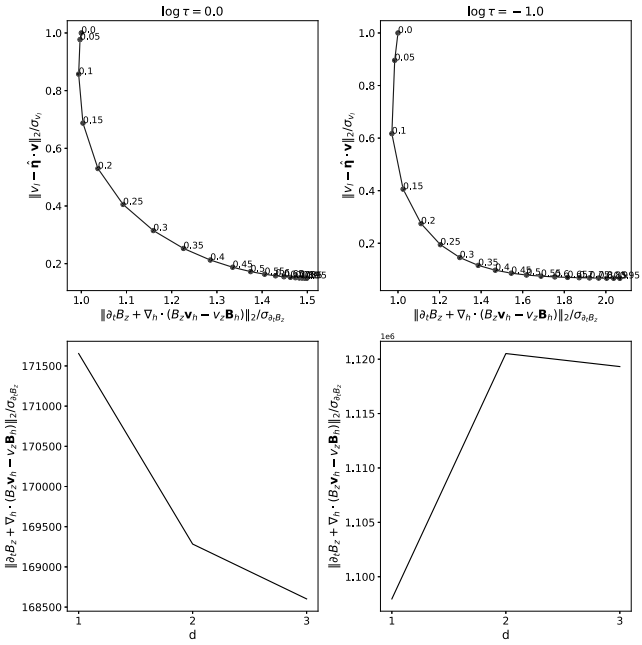

Figure 20. Same as Figure 19, but for the emulated observation.

inverse L and both L_1 and L_2 are small at large λ. Therefore we choose $\lambda = 1.0$.

We then choose the degree of Legendre expansion in the horizontal direction d by comparing the values of L_1 at different d. The variation of L_1 with respect to the degree of Legendre expansion in the horizontal direction d at the two layers is shown in the bottom panels of Figure 19. The degree of Legendre expansion in the vertical direction d_r is set as $d_r = d + 2$. At these two layers, we choose $d = 5$ and $d = 3$ because they have the smallest L_1.

A.2. DAVE4VMwDV on Emulated Observation

Figure 20 shows the L-curves with λ that varies from 0 to 1 for the application on the emulated observation at $\log\tau = 0$ and $\log\tau = -1$.

The L-curves for $\log\tau = 0$ and $\log\tau = -1$ have similar shapes: as the weighting λ increases, the Doppler residual L_2 decreases drastically first and then decreases at a slower pace, while the induction term L_1 has the inverse trend. A $\lambda = 0.35$ is finally selected for both heights as it provides a reasonable compromise: L_2 drops by factors of 3 and 5 as compared to DAVE4VM, while the increases in L_1 are only 25% and 35%, respectively.

The variation of L_1 with respect to the degree of Legendre expansion in the horizontal direction d at the two layers is shown in the bottom panels of Figure 20. The degree of Legendre expansion in the horizontal direction d_r is set to 5. The variation of L_1 for $d = [1, 2, 3]$ at $\log\tau = 0$ and $\log\tau = -1$ is plotted in Figure 20.

As shown in the left panel, at $\log\tau = 0.0$, L_1 decreases with respect to d and $d = 3$ gives the smallest value for L_1, suggesting the best fit for the induction equation. However, in the case of $\log\tau = -1.0$ (right panel), L_1 shows a different variation from the case of $\log\tau = 0.0$. In this case, $d = 1$ gives the best fit to the induction equation.

Appendix B
DAVE4VMwDV on Successive Frames

In the literature, the velocity is often estimated from two successive frames of observation to maximize the output cadence. For two frames at t_0 and $t_1 = t_0 + \Delta t$, where Δt is the cadence of the observation, the output is designated to the average time stamp, $t = t_0 + \Delta t/2$. The time derivative of a function f is calculated as

$$\left.\frac{\partial f}{\partial t}\right|_{t=t_0+\frac{\Delta t}{2}} = \frac{f(t_0+\Delta t) - f(t_0)}{\Delta t}. \tag{B1}$$

The input vector magnetograms and Doppler velocity are the average of two frames

$$f\left(t_0 + \frac{\Delta t}{2}\right) = \frac{f(t_0+\Delta t) + f(t_0)}{2}, \tag{B2}$$

where f can represent B_x, B_y, B_z, or v_l.

We posited earlier that the poor performance of DAVE4VMwDV might be due to the violation of the CFL condition. Our choice of temporal difference limits the time difference of the input at 4 s, twice that of the MURaM simulation snapshots. In this section, we apply DAVE4VMwDV on MURaM data at $t_0 = 32$ s and $t_1 = 34$ s, i.e., the highest possible cadence, to estimate the velocity at $t = 33$ s. For Poynting flux calculation, the other inputs are the average magnetogram and Dopplergram of these two time steps. We quantify the overall performance by evaluating the coefficients listed in Section 3.1. The ground-truth velocity is the averaged velocity from the simulation at t_0 and t_1.

Figure 21 shows the scatter plots between the inferred and the ground-truth velocities at the two optical depths. The inferred velocity at $\log\tau = 0$ has $E_{\rm rel} = 0.28$, $C = 0.96$, and $A = 0.95$, while the inferred velocity at $\log\tau = -1$ has $E_{\rm rel} = 0.23$, $C = 0.97$, and $A = 0.97$. Compared to the case with $\Delta t = 2$ s in Section 3.1, the performance is slightly increased. The slopes are closer to 1 for v_x and v_y. Similar to the findings in Section 3.3, the net shearing term of the Poynting flux is underestimated for both layers. The estimated net shearing Poynting flux can reproduce 70.0% and 57.8% of the ground truth at $\log\tau = 0$ and $\log\tau = -1$, respectively. The estimated net emergence Poynting flux can reproduce 98.5% and 90.4% of the ground truth at $\log\tau = 0$ and $\log\tau = -1$, respectively.

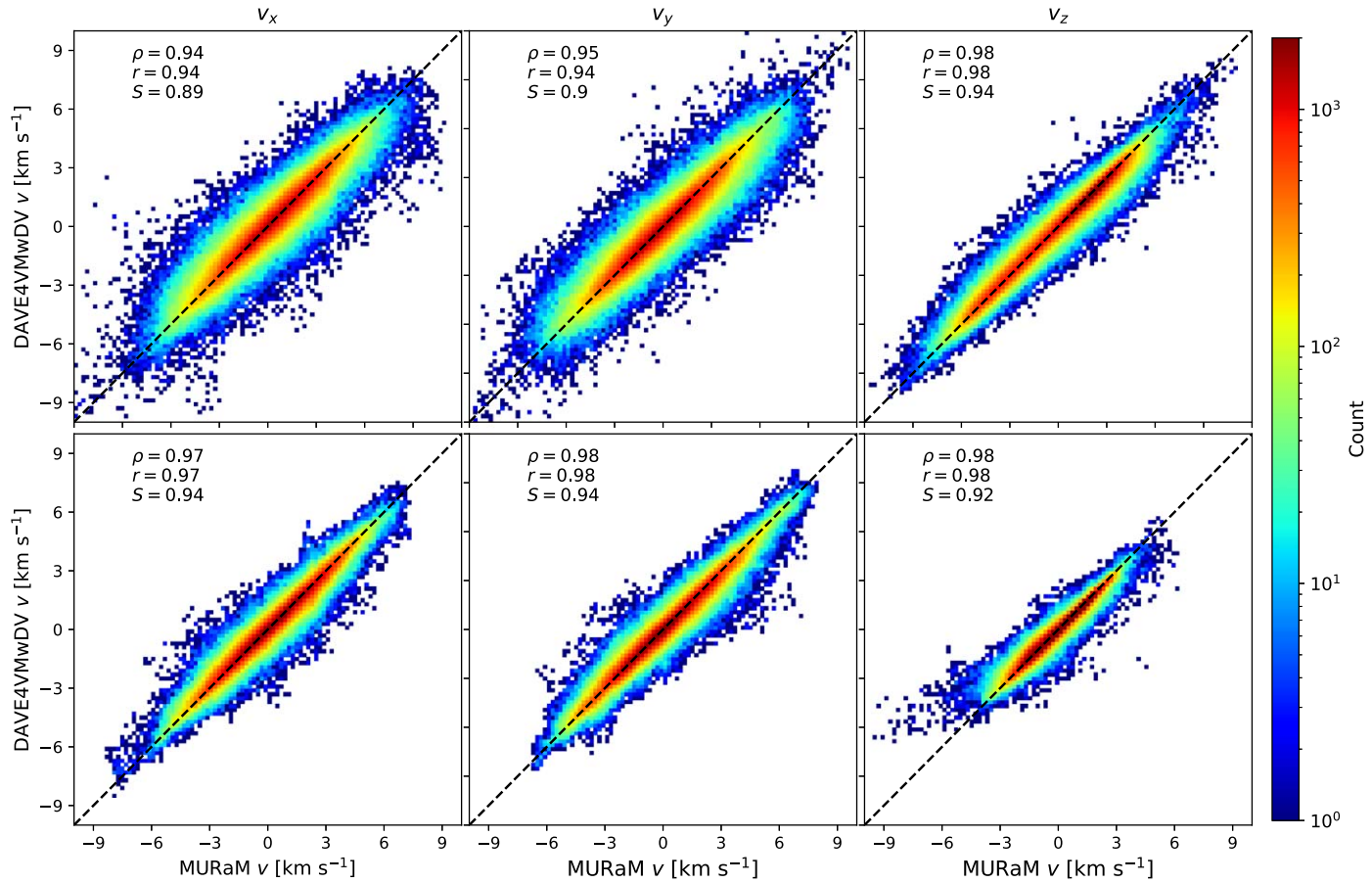

Figure 21. 2D histograms of the inferred velocity field and the reference velocity field at $\log\tau = 0$ (top) and $\log\tau = -1$ (bottom). From left to right, we show the histograms for v_x, v_y, and v_z. The Spearman coefficient (ρ), Pearson coefficient (r), and slope (S) are also shown on the plots.

ORCID iDs

Jiayi Liu (刘嘉奕) https://orcid.org/0000-0002-7290-0863
Xudong Sun (孙旭东) https://orcid.org/0000-0003-4043-616X
Peter W. Schuck https://orcid.org/0000-0003-1522-4632
Sarah A. Jaeggli https://orcid.org/0000-0001-5459-2628

References

Alissandrakis, C. E., & Gary, D. E. 2021, FrASS, 7, 77
Asensio Ramos, A., & Diaz Baso, C. J. 2019, A&A, 626, A102
Asensio Ramos, A., Requerey, I. S., & Vitas, N. 2017, A&A, 604, A11
Bellot Rubio, L., & Orozco Suárez, D. 2019, LRSP, 16, 1
Berghmans, D., Auchère, F., Long, D. M., et al. 2021, A&A, 656, L4
Danilovic, S., Schüssler, M., & Solanki, S. K. 2010, A&A, 513, A1
de Wijn, A. G., Lites, B. W., Berger, T. E., et al. 2008, ApJ, 684, 1469
del Toro Iniesta, J. C., & Ruiz Cobo, B. 2016, LRSP, 13, 4
Finley, A. J., Brun, A. S., Carlsson, M., et al. 2022, A&A, 665, A118
Fontenla, J. M., Avrett, E., Thuillier, G., & Harder, J. 2006, ApJ, 639, 441
Giannattasio, F., Consolini, G., Berrilli, F., & Moro, D. 2020, ApJ, 904, 7
Goic, M., Rubio, L. R. B., del Toro Iniesta, J. C., Surez, D. O., & Katsukawa, Y. 2016, ApJ, 820, 35
Goic, M., Rubio, L. R. B., Surez, D. O., Katsukawa, Y., & del Toro Iniesta, J. C. 2014, ApJ, 797, 49
Hale, G. E. 1908, ApJ, 28, 315
Hansen, P. C., & O'Leary, D. P. 1993, SJSC, 14, 1487
Jaeggli, S. A., Lin, H., Onaka, P., et al. 2022, SoPh, 297, 137
Jess, D. B., Jafarzadeh, S., Keys, P. H., et al. 2023, LRSP, 20, 1
Kusano, K., Maeshiro, T., Yokoyama, T., & Sakurai, T. 2002, ApJ, 577, 501
Leka, K. D., Barnes, G., Crouch, A. D., et al. 2009, SoPh, 260, 83
Liu, J., Sun, X., Schuck, P. W., et al. 2023, ApJ, 955, 40
Longcope, D. W. 2004, ApJ, 612, 1181
Metcalf, T. R. 1994, SoPh, 155, 235
Metcalf, T. R., Leka, K. D., Barnes, G., et al. 2006, SoPh, 237, 267
Milic, I., Centeno, R., Sun, X., Rempel, M., & de la Cruz Rodriguez, J. 2024, A&A, 683, A134
Moran, T., & Foukal, P. 1991, SoPh, 135, 179
Orozco Suárez, D., Bellot Rubio, L. R., Martìnez Pillet, V., et al. 2010, A&A, 522, A101
Pastor Yabar, A., Borrero, J. M., & Ruiz Cobo, B. 2019, A&A, 629, A24
Quintero Noda, C., Khomenko, E., Collados, M., et al. 2023, A&A, 675, A93
Rast, M. P., Bello González, N., Bellot Rubio, L., et al. 2021, SoPh, 296, 70
Rempel, M. 2014, ApJ, 789, 132
Rimmele, T. R., Warner, M., Keil, S. L., et al. 2020, SoPh, 295, 172
Ruiz Cobo, B., & del Toro Iniesta, J. C. 1992, ApJ, 398, 375
Schrijver, C. J., De Rosa, M. L., Metcalf, T. R., et al. 2006, SoPh, 235, 161
Schuck, P. W. 2006, ApJ, 646, 1358
Schuck, P. W. 2008, ApJ, 683, 1134
Tilipman, D., Kazachenko, M., Tremblay, B., et al. 2023, ApJ, 956, 83
Tremblay, B., & Attie, R. 2020, FrASS, 7, 25
van Noort, M. 2012, A&A, 548, A5
Vögler, A., Shelyag, S., Schüssler, M., et al. 2005, A&A, 429, 335
Welsch, B. T., Abbett, W. P., De Rosa, M. L., et al. 2007, ApJ, 670, 1434
Welsch, B. T., Fisher, G. H., Abbett, W. P., & Regnier, S. 2004, ApJ, 610, 1148
Yang, K. E., Tarr, L. A., Rempel, M., et al. 2024, ApJ, 976, 204
Zhou, G. P., Wang, J. X., & Jin, C. L. 2010, SoPh, 267, 63